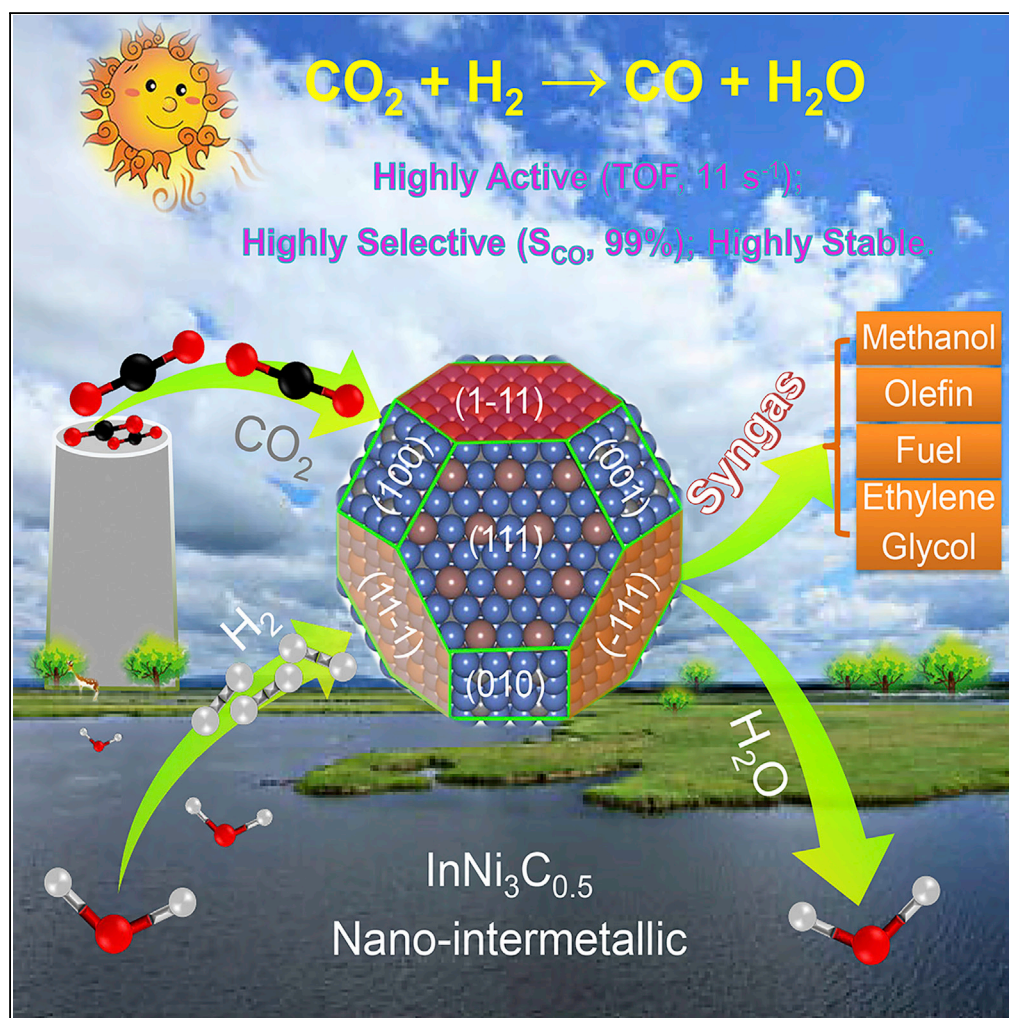


Article

Nano-Intermetallic $\text{InNi}_3\text{C}_{0.5}$ Compound Discovered as a Superior Catalyst for CO_2 Reutilization



Pengjing Chen,
Guofeng Zhao,
Xue-Rong Shi, Jian
Zhu, Jia Ding,
Yong Lu

gfzhao@chem.ecnu.edu.cn
(G.Z.)
shixuer05@mails.ucas.ac.cn
(X.-R.S.)
ylu@chem.ecnu.edu.cn (Y.L.)

HIGHLIGHTS

$\text{InNi}_3\text{C}_{0.5}$ catalyst is highly active, selective, and stable for the RWGS reaction

$\text{InNi}_3\text{C}_{0.5}(111)$ surface is gifted with dual active sites (3Ni-In and 3Ni-C)

CO_2 is dissociated into CO^* (preferentially desorbed) on 3Ni-C and O^* on 3Ni-In

$\text{InNi}_3\text{C}_{0.5}$ is also promising for application in carbonyl-to-hydroxyl processes

Chen et al., iScience 17, 315–324
July 26, 2019 © 2019 The Author(s).
<https://doi.org/10.1016/j.isci.2019.07.006>

Article

Nano-Intermetallic $\text{InNi}_3\text{C}_{0.5}$ Compound Discovered as a Superior Catalyst for CO_2 Reutilization

Pengjing Chen,^{1,5} Guofeng Zhao,^{2,5,*} Xue-Rong Shi,^{3,4,*} Jian Zhu,¹ Jia Ding,¹ and Yong Lu^{1,2,6,*}**SUMMARY**

CO_2 circular economy is urgently calling for the effective large-scale CO_2 reutilization technologies. The reverse water-gas shift (RWGS) reaction is the most techno-economically viable candidate for dealing with massive-volume CO_2 via downstream mature Fischer-Tropsch and methanol syntheses, but the desired groundbreaking catalyst represents a grand challenge. Here, we report the discovery of a nano-intermetallic $\text{InNi}_3\text{C}_{0.5}$ catalyst, for example, being particularly active, selective, and stable for the RWGS reaction. The $\text{InNi}_3\text{C}_{0.5}$ (111) surface is dominantly exposed and gifted with dual active sites (3Ni-In and 3Ni-C), which in synergy efficiently dissociate CO_2 into CO^* (on 3Ni-C) and O^* (on 3Ni-In). O^* can facilely react with 3Ni-C-offered H^* to form H_2O . Interestingly, CO^* is mainly desorbed at and above 400°C , whereas alternatively hydrogenated to CH_3OH highly selectively below 300°C . Moreover, this nano-intermetallic can also fully hydrogenate CO-derived dimethyl oxalate to ethylene glycol (commodity chemical) with high selectivity (above 96%) and favorable stability.

INTRODUCTION

Concerns about the vital global warming and ocean acidification problems caused by CO_2 excessive emission (Karl and Trenberth, 2003; Orr et al., 2005) have triggered extensive researches on its large-scale reutilization via effective, economical, and sustainable technologies for a CO_2 circular economy (Aresta et al., 2014; Porosoff et al., 2016). However, industrialized CO_2 reutilization is just limited to the synthesis of urea and polycarbonate (occupying only 0.5% [Shima et al., 2012; Su et al., 2017] of CO_2 emissions), whereas enzymatic and electro-/photo-chemical strategies are hampered by their low CO_2 -conversion efficiency (Wang et al., 2008; Kondratenko et al., 2013). To achieve the large-scale CO_2 reutilization, CO_2 hydrogenation with renewable-energy-generated H_2 to CO by the reverse water-gas shift (RWGS) reaction is the most techno-economically viable candidate (Porosoff et al., 2016; Kondratenko et al., 2013; Xu and Moulijn, 1996; Porosoff and Chen, 2013; Zhang et al., 2017), thanks not only to its high efficiency, enabling to deal with vast amounts of CO_2 , but also to the great versatility of syngas ($\text{CO} + \text{H}_2$, product gas of RWGS reaction) to produce commodity chemicals and fuels (occupying 40% CO_2 emissions [Zhang et al., 2017] via mature Fischer-Tropsch and methanol (CH_3OH) syntheses [Porosoff et al., 2016; Kondrat et al., 2016]).

The RWGS reaction is an equilibrium-limited endothermic reaction (required enthalpy of $41.17 \text{ kJ mol}^{-1}$). According to Le Châtelier's principle, high-temperature (about $400\text{--}800^\circ\text{C}$) thermodynamically favors high CO_2 conversion and high CO selectivity, but the undesired methanation also proceeds under the preferred RWGS conditions (Chen et al., 2001; Wu et al., 2015; Gonçalves et al., 2017; Yang et al., 2017). Therefore, a techno-economically available catalyst with outstanding CO_2 -to-syngas performance is the prerequisite for the large-scale RWGS implementation. To date, homogeneous complexes and heterogeneous solids catalysts have been extensively explored. The homogeneous catalysts show satisfactory activity and selectivity (Federsel et al., 2010), but their difficult recovery from the reaction mixture makes them unattractive. The heterogeneous catalysts are more competitive in terms of ready catalyst-product separation and continuous processes. They mainly include the nanoparticles of precious metals (e.g., Au, Ag, Pt) (Porosoff et al., 2016; Yang et al., 2017) and non-precious metals (e.g., Cu, Ni) (Zhang et al., 2017; Chen et al., 2001; Wu et al., 2015; Gonçalves et al., 2017) dispersed on supports (e.g., SiO_2 , Al_2O_3 , CeO_2 , MoC_x) (Porosoff et al., 2016; Zhang et al., 2017; Chen et al., 2001; Wu et al., 2015; Gonçalves et al., 2017; Yang et al., 2017). Despite the excellent RWGS activity, the precious-metal catalysts suffer from their limited natural abundance. Cu and Ni catalysts are intensively studied but are not promising owing to either serious sintering (Cu) (Zhang et al., 2017; Chen et al., 2001) or high methanation activity (Ni) (Wu et al., 2015; Gonçalves et al.,

¹Shanghai Key Laboratory of Green Chemistry and Chemical Processes, East China Normal University, Shanghai 200062, China

²School of Chemistry and Molecular Engineering, East China Normal University, Shanghai 200062, China

³Department of Materials Engineering, Shanghai University of Engineering Science, Shanghai 201620, China

⁴Institute of Physical Chemistry, University of Innsbruck, Innrain 80-82, Innsbruck, Austria

⁵These authors contributed equally

⁶Lead Contact

*Correspondence: gzhao@chem.ecnu.edu.cn (G.Z.), shixuer05@mails.ucas.ac.cn (X.-R.S.), ylu@chem.ecnu.edu.cn (Y.L.)

<https://doi.org/10.1016/j.isci.2019.07.006>



2017). Given the chemical inertness of CO₂ molecule (Xu and Moulijn, 1996), the heart of RWGS is to exquisitely design and tailor a groundbreaking catalytic material with both high efficiency and low cost, but this represents a grand challenge within the CO₂-conversion field.

Against all odds, the tantalizing progresses in nano-intermetallic catalysis (Stamenkovic et al., 2007; Studt et al., 2014) open an opportunity for designing and tailoring qualified RWGS catalysts because nano-intermetallic has fascinating prospects in catalysis field, with their tunable components and ratios, variable constructions, and reconfigurable electronic structures, distinctly different from their single metals (Stamenkovic et al., 2007; Armbrüster et al., 2012; Ji et al., 2010). Particularly, their precise atomic ordering structure can provide rational predictions of the effects of geometry and electronic structure on their catalytic properties for required reactions (Wang et al., 2013; Nicholson et al., 2014; Qin et al., 2018). One of the recent pertinent examples is the discovery of a Ni₅Ga₃ nano-intermetallic, which strikingly shows that the Ni, originally active for CO₂ methanation, turns itself suddenly into a qualified CO₂-to-CH₃OH catalyst after Ga alloying (Studt et al., 2014), because this intermetallic offers the unique Ga-rich sites for CH₃OH formation. Encouraged by these big achievements toward nano-intermetallic catalysis, we believe that the nano-intermetallic can pave a road to the rational engineering of more intelligent catalysts gifted with flexibly arranged atomic structures and tailor-made catalytic properties for the RWGS reaction as well as other reactions for CO₂ reutilization.

Here, we present a nano-intermetallic InNi₃C_{0.5} catalyst that is particularly active, selective, and stable for the RWGS reaction under extremely wide reaction conditions. Such nano-intermetallic is fabricated via carburizing the In-Ni nano-intermetallic in the real RWGS stream and is gifted with dual active sites (i.e., 3Ni-In and 3Ni-C) on the InNi₃C_{0.5}(111) surface. The dual sites act in synergy to facilitate dissociate CO₂* (adsorbed on 3Ni-In sites) into CO* (on 3Ni-C sites) and O* (on 3Ni-In sites), and the O* can favorably react with 3Ni-C offered H* to form H₂O. Most notably, the CO* is mainly desorbed into gas phase at and above 400°C but can be highly selectively hydrogenated to form CH₃OH below 300°C with a promising CO₂-to-CH₃OH capacity. Furthermore, this nano-intermetallic can fully hydrogenate dimethyl oxalate (obtainable from oxidative coupling of CO (Fenton and Steinwand, 1974), product of the RWGS) to ethylene glycol (a commodity chemical) with high selectivity (above 96%) and favorable stability.

RESULTS

Discovery of InNi₃C_{0.5} and Its Application for RWGS Reaction

To exquisitely tailor a groundbreaking RWGS catalyst, the elaborate choice of appropriate elements oriented by this reaction should be initially conducted but poses a great challenge because the relevant elements for this reaction traverse most of the periodic table. The first metal that mostly attracts attention is Ni, because Ni-based catalysts are typically used for the RWGS reaction despite CH₄ formation (Wu et al., 2015; Gonçalves et al., 2017). Moreover, In is another attractive element, because In-based catalysts are burgeoning in CO₂ conversion (Ye et al., 2012; Park et al., 2017; Larrazábal et al., 2016), and, for example, the intermetallic AgIn catalyst is highly efficient for electrochemical reduction of CO₂ to CO (Park et al., 2017; Larrazábal et al., 2016). We thus surmise that In-Ni intermetallic could reconstruct geometric-electronic structures of Ni, which might be feasible to switch Ni catalysis in CO₂ reduction from CH₄ formation to CO formation.

A series of pure intermetallics of InNi, InNi₂, and InNi₃ were successfully synthesized (Figure 1A) and then were evaluated for the RWGS reaction. Comparison with the conventional Cu-based catalysts (Zhang et al., 2017; Chen et al., 2001) reveals that the intermetallic In-Ni catalysts deliver exciting intrinsic RWGS performances, especially for InNi₃ with a high CO formation rate of 1.96 mmol g_{cat}⁻¹ min⁻¹ and a considerably low CH₄ selectivity (Figure S1). It is very intriguing to find that after reaction the InNi, InNi₂, and InNi₃ phases are *in situ* changed in association with a new phase formation of InNi₃C_{0.5} (Figure 1B, identified in following section). Consistently, the InNi₃C_{0.5} formation is thermodynamically favorable with large ordering energy (such as 2.72 eV for InNi₃ carburization with CO, Figure S2), which also portends that the InNi₃C_{0.5} is stable under the RWGS conditions. Notably, only InNi₃ could be fully transformed into pure InNi₃C_{0.5} owing to the identical stoichiometric In:Ni ratios of 1:3 and offers the highest RWGS performance, indicating that InNi₃C_{0.5} should be responsible for the RWGS reaction.

The above-mentioned results and analyses make us confident that the InNi₃C_{0.5} intermetallic is a superior RWGS catalyst. To make it a practical catalyst, the thin-felt Al₂O₃/Al-fiber substrate consisting of 10 vol%

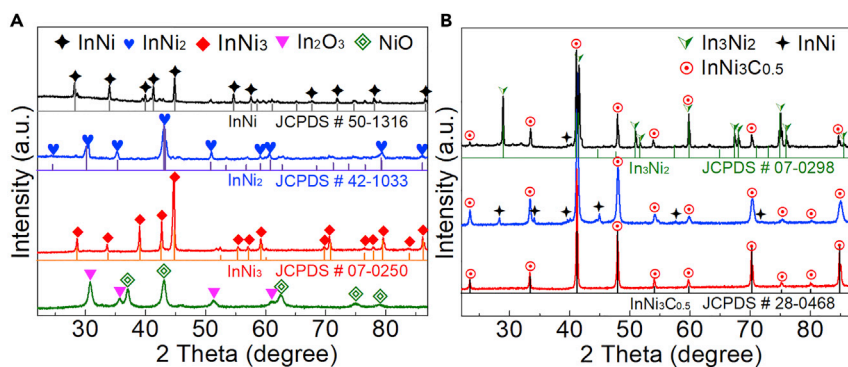


Figure 1. XRD Patterns of the Various Catalysts

(A) In_2O_3 -NiO mixture (green) and In-Ni intermetallics with different In:Ni molar ratio (InNi, black; InNi_2 , blue; InNi_3 , red). (B) Used intermetallics of InNi (black), InNi_2 (blue), and InNi_3 (red) after the RWGS reaction (500°C , GHSV of $30,000 \text{ mL g}_{\text{cat}}^{-1} \text{ h}^{-1}$, $\text{H}_2/\text{CO}_2/\text{N}_2$ molar ratio of 66/22/12, 0.1 MPa).

$60\text{-}\mu\text{m}$ $\text{Al}_2\text{O}_3/\text{Al}$ -fiber and 90 vol% voidage (Wang et al., 2016) was used to support 9 wt% $\text{InNi}_3\text{C}_{0.5}$. This strategy permits the engineering of $\text{InNi}_3\text{C}_{0.5}$ nano-intermetallic at “nano-meso-macro” triple-scale levels of both porosity and structure in one step (Figures 2A–2C, S3A, and S3B), thereby making the catalyst development and reaction engineering (for enhanced heat/mass transfer) go hand in hand (Wang et al., 2016; Li et al., 2015). The $\text{InNi}_3\text{C}_{0.5}/\text{Al}_2\text{O}_3/\text{Al}$ -fiber catalyst was tested for the RWGS reaction in a tubular fixed-bed reactor. As expected, this catalyst always achieves high CO_2 conversions very close to the thermodynamic equilibrium values with above 97% CO selectivity under the wide reaction conditions (Figures 2D–2F). For example, a 53% CO_2 conversion is obtainable, quite close to the equilibrium value of 54%, at 540°C and a gas hourly space velocity (GHSV) of $54,000 \text{ mL g}_{\text{cat}}^{-1} \text{ h}^{-1}$. This catalyst delivers a very high intrinsic activity with a turnover frequency (TOF) of 11.0 CO per active site per second at 540°C (see detailed TOF calculation in Supplemental Information), almost one to two orders of magnitude higher than that seen with most platinum/oxide and non-noble-metal catalysts (Table S1). Furthermore, a kinetic study was carried out over the $\text{InNi}_3\text{C}_{0.5}/\text{Al}_2\text{O}_3/\text{Al}$ -fiber catalyst, and the apparent activation energy was calculated with the result as shown in Figure S3D. $\text{InNi}_3\text{C}_{0.5}/\text{Al}_2\text{O}_3/\text{Al}$ -fiber provided a much lower E_a (60 kJ/mol) than Cu/ZnO-based catalysts (112 kJ/mol, Schumann et al., 2015), further indicating that this catalyst has a high intrinsic activity. Also encouraging is the exclusive CO selectivity (above 98%) with pressure increasing from 1.0 to 4.0 MPa at 540°C (Figure 2F), despite the fact that CH_4 formation is much favorable at high pressure over the conventional Ni-based catalysts (Wu et al., 2015; Gonçalves et al., 2017; Li et al., 2015).

Stability is a significant consideration for catalysts in practical applications. Our $\text{InNi}_3\text{C}_{0.5}/\text{Al}_2\text{O}_3/\text{Al}$ -fiber catalyst is very stable with 52%–53% CO_2 conversion and 97%–99% CO selectivity throughout the entire 150 h testing at a GHSV of $54,000 \text{ mL g}_{\text{cat}}^{-1} \text{ h}^{-1}$ and 540°C (Figure 2G). Even at a high GHSV of $300,000 \text{ mL g}_{\text{cat}}^{-1} \text{ h}^{-1}$ and 600°C , the $\text{InNi}_3\text{C}_{0.5}/\text{Al}_2\text{O}_3/\text{Al}$ -fiber catalyst also shows a high stability with no deactivation sign throughout 65 h testing (Figure 2H). In comparison, the Cu/ β - Mo_2C catalyst maintains 85% of its initial activity after 40 h reaction and the Cu/ZnO/ Al_2O_3 catalyst loses more than 60% of its initial activity within 15 h reaction under the identical reaction conditions (Zhang et al., 2017). It is not surprising that the $\text{InNi}_3\text{C}_{0.5}$ crystalline phase, surface morphology, and structure of the used catalysts are preserved unchanged (Figures S3E–S3H), consistent with the excellent activity/selectivity maintenance in Figures 2G and 2H. To the best of our knowledge, the $\text{InNi}_3\text{C}_{0.5}$ intermetallic has never been used before for any application in catalysis, and herein we discover its superior RWGS performance—including CO_2 conversion, CO selectivity, and especially high-temperature stability—over the reported state-of-the-art catalysts (Table S1).

Structure Identification

To definitely identify the crystal structure and composition of the as-formed carbide-intermetallic from In-Ni intermetallics, such pure carbide-intermetallic was synthesized via fully carburizing InNi_3 , and its X-ray diffraction (XRD) pattern completely coincides with the one of $\text{InNi}_3\text{C}_{0.5}$ that has an anti-perovskite-type structure (Joint Committee on Powder Diffraction File No. 28-0468; Figure 3A and Table S2).

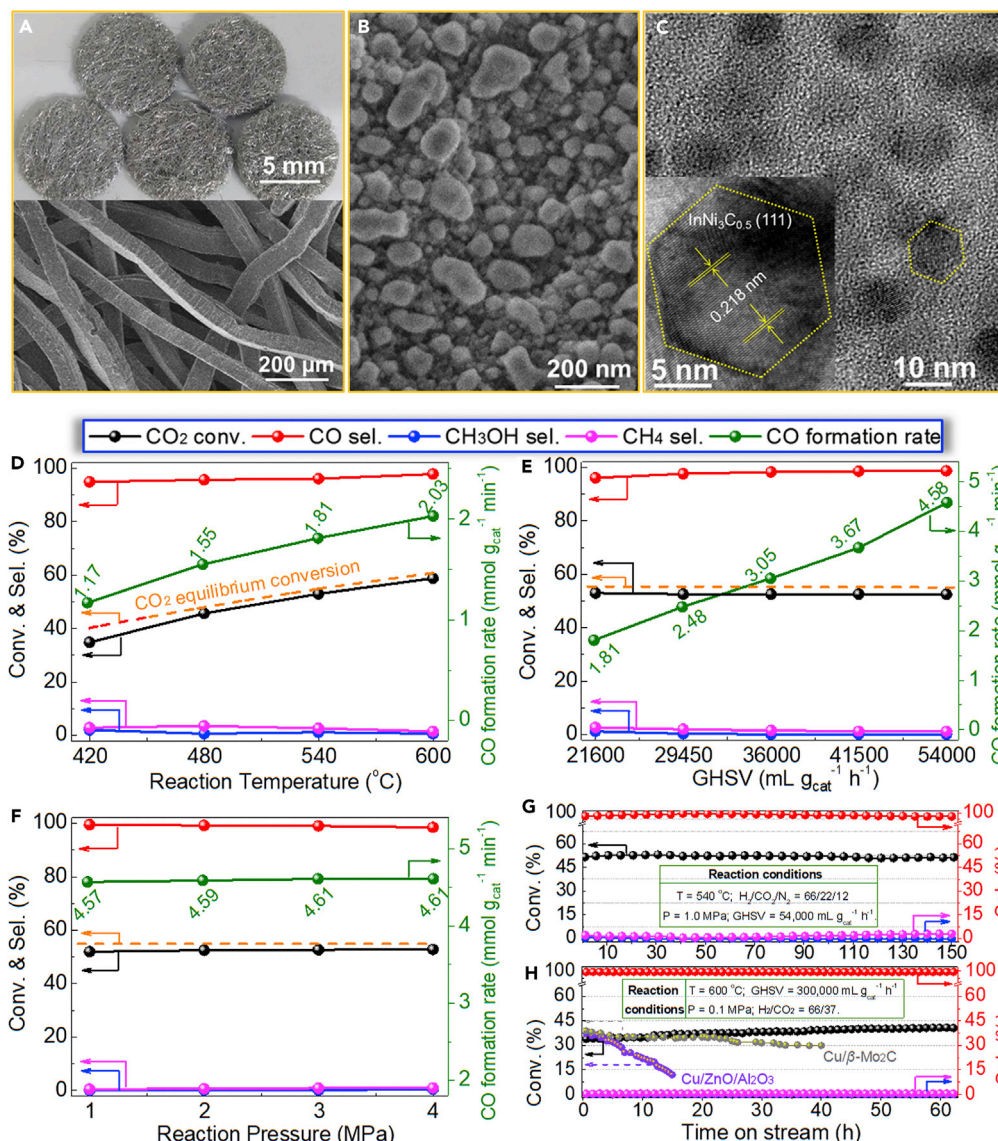


Figure 2. Structural and Morphological Features of the InNi₃C_{0.5}/Al₂O₃/Al-fiber Catalyst and Its RWGS Performance

(A) Optical photograph (top) and scanning electron microscopy (SEM) image (bottom) of the fresh catalyst.

(B) High-magnification SEM image of the fresh catalyst.

(C) TEM images of the fresh catalyst (inset: lattice fringes with distance of 0.218 nm corresponding to the InNi₃C_{0.5}(111) surface).

(D–F) CO₂ conversion, product selectivity, and CO-formation rate as a function of (D) reaction temperature (at a GHSV of 21,600 mL g_{cat}⁻¹ h⁻¹ and 4.0 MPa), (E) GHSV (at 540 °C and 4.0 MPa), and (F) reaction pressure (at a GHSV of 54,000 mL g_{cat}⁻¹ h⁻¹ and 540 °C) for a feed gas of H₂/CO₂/N₂ with molar ratio of 66/22/12.

(G and H) Time on stream under different reaction conditions and comparison (H) with the reported literature data over the commercial Cu/ZnO/Al₂O₃ (Zhang et al., 2017) and Cu/β-Mo₂C (Zhang et al., 2017) catalysts.

Moreover, the In:Ni:C molar ratio of the as-synthesized InNi₃C_{0.5} was determined to be 1:2.99:0.49 (see elemental analyses in Supplemental Information), quite close to its stoichiometric ratio. Figure 3B shows its structural model containing eight InNi₃ units. For each unit, eight In atoms occupy the eight corners and six Ni atoms occupy the six face centers; four C atoms randomly disperse in these eight body centers, but with the most stable configuration in a regular tetrahedron (Figure S4). The Wulff equilibrium shape of the InNi₃C_{0.5} nanocrystal was further optimized, and its optimum shape exposes fourteen surfaces

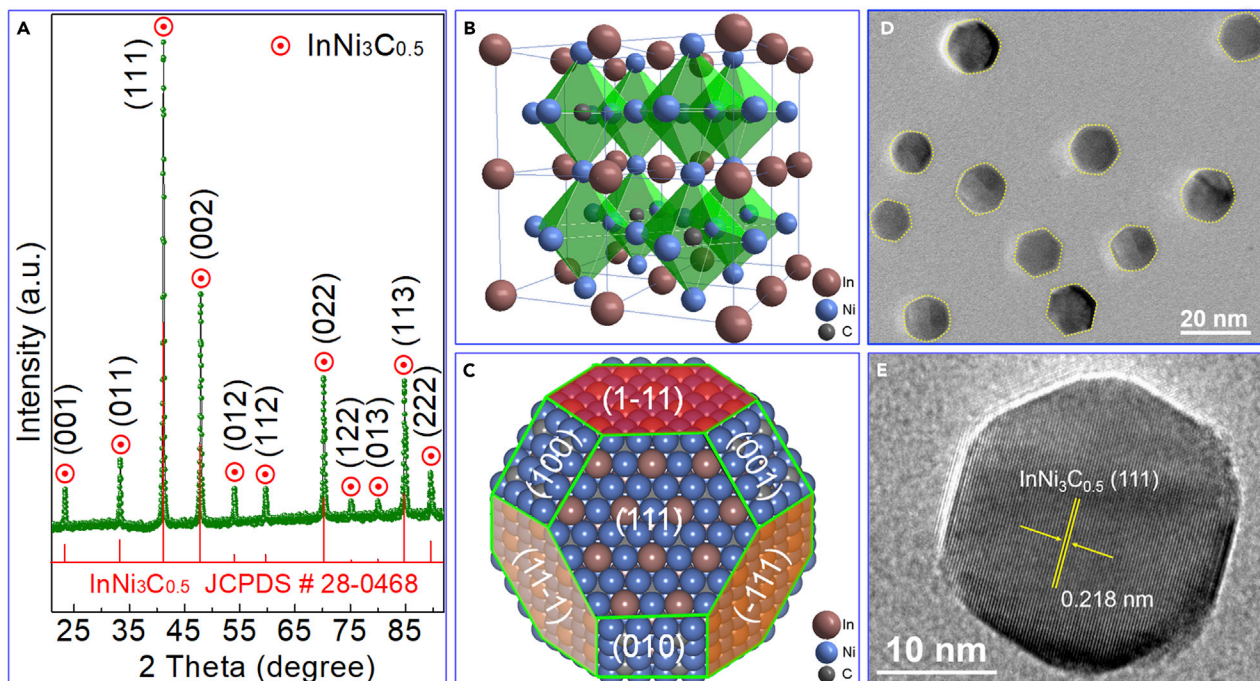


Figure 3. Structure and Morphology of the $\text{InNi}_3\text{C}_{0.5}$ Nano-Intermetallic

(A) XRD pattern of the as-synthesized $\text{InNi}_3\text{C}_{0.5}$ nano-intermetallic.

(B) Ball-and-stick perspective of polyhedral $\text{InNi}_3\text{C}_{0.5}$ ($a \times 2 \times 2$ super cell) with cubic ($Fm\bar{3}m$) anti-perovskite-type structure (green octahedron, C-Ni₆).

(C) Optimum Wulff equilibrium shape of $\text{InNi}_3\text{C}_{0.5}$ crystal.

(D) TEM image of the as-synthesized $\text{InNi}_3\text{C}_{0.5}$ nano-intermetallic, showing its uniform hexagonal shape (marked by yellow dashed lines).

(E) High-resolution TEM image of a typical $\text{InNi}_3\text{C}_{0.5}$ nanoparticle with hexagonal shape and a lattice spacing of 0.218 nm corresponding to the $\text{InNi}_3\text{C}_{0.5}(111)$ surface.

consisting of eight hexagons and six squares (Figure 3C). The $\text{InNi}_3\text{C}_{0.5}(111)$ is the most stable surface of the hexagonal shapes with the lowest surface free energy (Table S3). Interestingly, high-resolution transmission electron microscopy (TEM) also displays an approximate hexagonal morphology of the real synthetic $\text{InNi}_3\text{C}_{0.5}$ nanoparticles (Figures 3D, 3E, and S5), and the lattice spacing of 0.218 nm is assignable to the $\text{InNi}_3\text{C}_{0.5}(111)$ surface.

Theoretical Calculations Study

In the last decade, significant advances have been achieved in the atomistic-theoretical calculations, enabling us to computationally construct molecular and crystalline structures and to reveal the reaction pathways on the catalyst surface at atomic-molecular level (Nicholson et al., 2014; Qin et al., 2018; Studt et al., 2014; Mao et al., 2017). Therefore, the RWGS reaction mechanism on $\text{InNi}_3\text{C}_{0.5}$ is first investigated by the density functional theory (DFT) calculations. We selected the most stable $\text{InNi}_3\text{C}_{0.5}(111)$ as the ideal surface and established the dual active sites (h1: $\text{Hollow}_{(3\text{Ni}-\text{In})}$; h2: $\text{Hollow}_{(3\text{Ni}-\text{C})}$; Figure 4A) from nine kinds of possible active sites (see detailed results in Table S4). As shown in Figure 4B, the CO_2 molecule is chemically adsorbed via a bending configuration to form CO_2^* on h1 site, and the H_2 molecule spontaneously dissociates into H^* that can be adsorbed on both h1 and h2 sites. Electron density distribution for the dual active sites is richer than the others, which makes them more nucleophilic and more favorable for CO_2 activation (Figure S6). Therefore, the CO_2^* readily dissociates into CO^* adsorbed on h2 site and O^* adsorbed on h1 site with moderate exothermicity (namely, reaction energy E_r , -0.38 eV) and a low activation barrier (E_a , 0.32 eV), but with higher E_a of CO_2^* hydrogenation to formate (HCOO^* , 0.42 eV) and to carboxyl (COOH^* , 0.75 eV, Figure S7 and Table S5). Clearly, the CO_2^* dissociation to CO^* and O^* (i.e., redox pathway) is preferred over the formate and carboxyl pathways on the $\text{InNi}_3\text{C}_{0.5}(111)$ surface. Furthermore, the formed O^* on h1 site preferably reacts with H^* on the neighboring h2 site to produce an OH^* group (E_a , 0.73 eV), and subsequently, two OH^* groups on the dual sites are easily transformed into H_2O^* (E_a , 0.25 eV) that is finally desorbed into the gas phase (E_a , 0.35 eV). The dual active

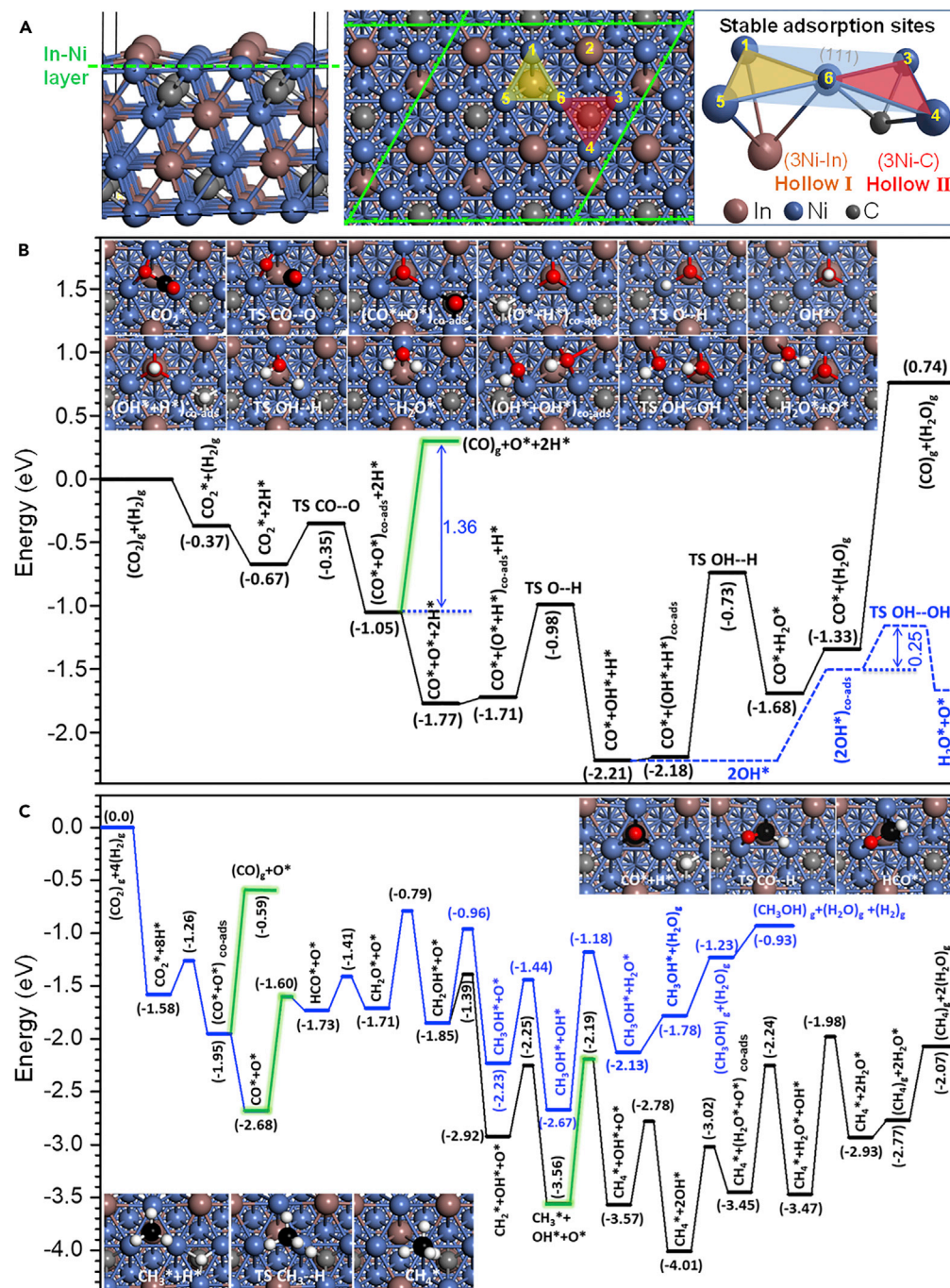


Figure 4. Dual Active Sites and Reaction Pathways for CO_2 Hydrogenation on the $\text{InNi}_3\text{Co}_{0.5}(111)$ Surface

(A) Side (left) and top (middle) views of the $\text{InNi}_3\text{Co}_{0.5}(111)$ surface, and detailed structure (right) of the dual active sites of "3Ni-In" (i.e., Hollow I by three Ni atoms and one In atom) and "3Ni-C" (i.e., Hollow II by three Ni atoms and one C atom). (B and C) Energy profiles on the $\text{InNi}_3\text{Co}_{0.5}(111)$ surface for (B) the most favorable pathways to RWGS reaction and for (C) the competitive pathways for CO_2 hydrogenation to CO (green), CH_3OH (blue), and CH_4 (black), where the black, red, and white balls represent the C, O, and H atoms in the reactive species, respectively.

sites provide much lower E_a than the sole h1 sites for the above-mentioned steps (see detailed results in Table S5), probably the consequences of appropriate adsorption of reaction intermediates in terms of their adsorption strength (Table S4) and the distance between them (the dual active sites have shorter

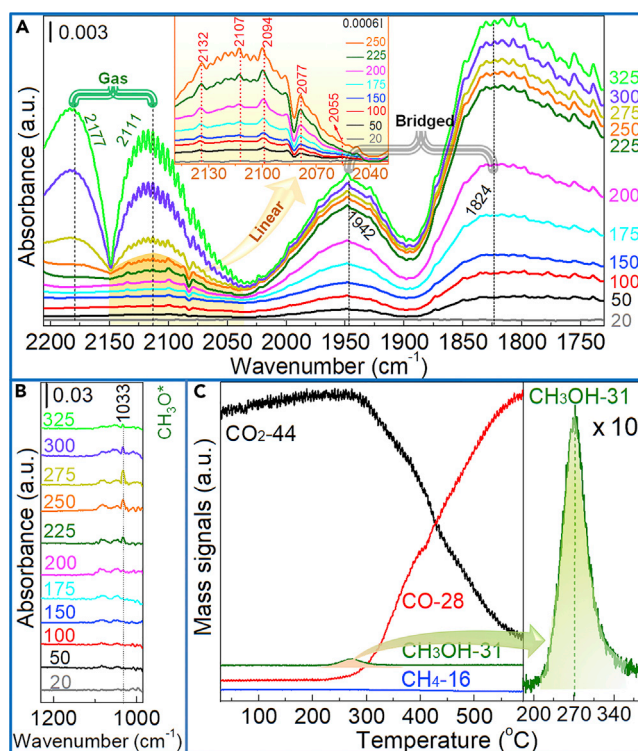


Figure 5. *In Situ* FTIR and On-line Mass Spectrometric Analyses of CO₂ Hydrogenation on the InNi₃C_{0.5} Catalyst (A and B) *In situ* FTIR spectra of CO₂ hydrogenation against reaction temperature on the InNi₃C_{0.5} catalyst in wavenumber range of (A) 2,210–1,730 cm⁻¹ and (B) 1,230–980 cm⁻¹. (C) Mass spectrometric signals of the carbonaceous species for CO₂ hydrogenation: CO₂ signal (m/z = 44), CH₃OH signal (m/z = 31), CO signal (m/z = 28), and CH₄ signal (m/z = 16).

adjacent h1-h2 distance of 3.106 Å than the sole h1 sites with an adjacent h1-h1 distance of 5.345 Å, Figure 4A). In contrast, CO₂* dissociation on Cu(111) becomes endothermic (E_r , +1.06 eV, thermodynamically unfavorable) and is kinetically unfavorable (E_a of 1.55 eV versus 0.32 eV on InNi₃C_{0.5}(111), Figures 4B, S8, and S9).

The formed CO* either undergoes further hydrogenation to CH₄ and/or CH₃OH or desorbs into the gas phase. Figure 4C shows that CO* desorption overcomes a slightly higher E_a of 1.36 eV at 0 K than the formation of CH₄ (CH₃*-to-CH₄*, 1.27 eV) and CH₃OH (CO*-to-HCO*, 1.05 eV), clearly exhibiting a possibility of CH₃OH formation (see detailed results and discussion in Figures S10 and S11). It should be noted, however, that CO* desorption is thermodynamically more favorable at elevated temperatures (Figures S12 and S13) owing to the significant entropy contributions (Graciani et al., 2014), and therefore CO* is preferentially desorbed into gas phase rather than hydrogenated to CH₃OH at our real RWGS temperature of 420°C–600°C (see experimental results in Figures 2D–2F).

Infrared Spectroscopy Study

To verify the RWGS reaction pathway on InNi₃C_{0.5} from experimental perspective, the *in situ* Fourier transform infrared (FTIR) spectroscopy analysis was carried out on pure InNi₃C_{0.5} in a continuous H₂/CO₂/N₂ (molar ratio of 66/22/12) flow at ambient pressure. As shown in Figure 5A, the linear adsorbed CO* species are formed from CO₂ dissociation even at 50°C, evidenced by infrared (IR) bands (Martin et al., 2016) at 2132, 2107, 2094, 2077, and 2055 cm⁻¹. Along with the increase in the temperature, the IR band intensity of linear adsorbed CO* becomes slightly stronger from 50°C to 175°C, remains almost unchanged from 200°C to 250°C, and then diminishes until disappearance at 325°C. In addition, two new bands at 1942 and 1824 cm⁻¹ assignable to the bridge-absorbed CO* species (Dou et al., 2017) are observed at 100°C while becoming stronger and stronger along with the temperature. Plentiful gaseous CO starts to be detected only at 300°C, and its formation is favored with the temperature. Neither CH₄ (at 3013 cm⁻¹)

Substrate	Target Product	T (°C)	P (MPa)	WHSV ^a (h ⁻¹)	Conv. (%)	Sel. (%)
DMO	EG	210	2.5	0.44	100/100 ^b	96.0/96.1 ^b
Acetone	Isopropanol	150	0.1	6.0	65.3	>99
Furfural	Furfuryl alcohol	180	0.5	0.7	98.3	91.0
Cyclohexanone	Cyclohexanol	170	0.1	6.0	62.6	>99
Butanone	Butanol	120	0.1	5.0	57.3	98.1
Salicylaldehyde	Salicylol	350	0.1	8.0	67.4	97.2
<i>n</i> -Nonaldehyde	<i>n</i> -Nonyl alcohol	300	0.1	7.0	56.0	95.1

Table 1. Hydrogenation of Carbonyl Compounds Catalyzed by the InNi₃C_{0.5}/Ni-foam Catalyst

The molar ratio of H₂ to DMO is 135, and the ratios of H₂ to other substrates are 10. The by-products selectivities were summarized in Table S7.

^aWeight hourly space velocity (WHSV) of substrates.

^bDMO conversion and EG selectivity after 500 h reaction.

(Dou et al., 2017) nor formate and carboxyl species (at 1281 and 1360–1600 cm⁻¹) (Dou et al., 2017) are detectable in the whole temperature range studied, coinciding with the DFT-suggested preferable formation of CO over CH₄, formate, and carboxyl. It should be also noticed that no adsorbed CO₂* species are detectable; a possible explanation is that the CO₂ adsorption-dissociation is too fast to be monitored by IR, also coinciding with the DFT-indicated very low E_a of only 0.32 eV for CO₂* dissociation. These IR spectra undoubtedly validate the DFT results: CO₂ can be efficiently converted to CO via redox pathway rather than formate and carboxyl ones.

Moreover, DFT calculations on InNi₃C_{0.5}(111) surface predict the possibility of CH₃OH formation (Figures 4C and S10 and Table S5). CO* is first hydrogenated into HCO* (E_a, 1.05 eV), which is easily hydrogenated into CH₂O* (E_a, 0.32 eV); CH₂O* can be continuously hydrogenated into CH₂OH* (E_a, 0.65 eV) or CH₃O* (E_a, 0.60 eV); however, CH₂OH* is more favorably hydrogenated into CH₃OH* (E_a, 0.88 eV) over CH₃O* to CH₃OH* (E_a, 1.71 eV). Therefore, we infer that CH₃O* should be detectable by IR owing to its high accumulation and that CH₃OH can be formed through the CO*-to-HCO*-to-CH₂O*-to-CH₂OH*-to-CH₃OH* pathway (see detailed results and discussion in Figure S10). Indeed, CH₃O* with IR band at 1033 cm⁻¹ are detectable at 200°C–325°C (Figure 5B), whereas CH₃OH is detected by the on-line mass spectrometry (MS) at 220°C–310°C accompanied by gaseous CO formation above 300°C (Figure 5C). Notably, the absence of CH₂O* and CH₂OH* in *in situ* IR spectra is probably a consequence of the low residence time of these species on the surface under atmospheric conditions (Graciani et al., 2014). These IR and MS spectra consistently display that CO* is hydrogenated into CH₃OH highly selectively below 300°C, whereas it is dominantly desorbed into gas phase above 300°C.

Extended Application for CO₂-to-CH₃OH and Carbonyl-to-Hydroxyl Transformations

The above-mentioned DFT and FTIR results also make us confident that the InNi₃C_{0.5} nano-intermetallic is a potential catalyst for the CO₂ hydrogenation to CH₃OH, which becomes more and more competing in recent years. With reaction temperature reduced from 400°C–600°C (for the RWGS reaction) to 300°C and below, the InNi₃C_{0.5}/Al₂O₃/Al-fiber indeed turns itself suddenly into a CO₂-to-CH₃OH catalyst, being capable of converting 1%–8% CO₂ into CH₃OH with 60%–98% selectivity (corresponding to the CH₃OH space time yield of 70–330 g_{MeOH} kg_{cat}⁻¹ h⁻¹) at 200°C–300°C (Table S6). The preferable CH₃OH formation rather than CO formation below 300°C is attributed to the fact that low temperatures thermodynamically favor further hydrogenation of CO* to CH₃OH* (Figures S12 and S13). These results exhibit an interesting temperature-dependent selectivity switching for CO₂ hydrogenation.

Moreover, in the light that CO₂ molecule has the carbonyl property and InNi₃C_{0.5} intermetallic can efficiently activate CO₂ molecule, we wonder whether this catalyst is favorable for other carbonyl-compounds transformation, such as the hydrogenation of aldehydes/ketones/esters to corresponding alcohols. To avoid the adverse influence of acid groups on the surface of Al₂O₃, we directly supported the InNi₃C_{0.5} nano-intermetallic onto a thin-sheet Ni-foam substrate with 110 pores per inch (Figure S14, see detailed preparation in Supplemental Information). Indeed, the InNi₃C_{0.5}/Ni-foam catalyst presents the satisfying activity and high product selectivity (Tables 1 and S7), providing the general and efficient ability to activate the C=O bond for

carbonyl-to-hydroxyl transformation. Notably, ethylene glycol (EG) is an important commodity chemical, used for polyester manufacture, anti-freeze compounds, and solvents (Yue et al., 2012), and the gas-phase hydrogenation of dimethyl oxalate (DMO) to EG (its commercialization is on the way) is an attractive alternative EG synthesis using syngas (Fenton and Steinwand, 1974) derived from non-oil resources (such as coal, natural gas, and biomass) even from CO₂ through the RWGS reaction. This foam-structured catalyst is capable of completely converting DMO at a high EG selectivity of 96% with a promising stability (Table 1). Moreover, the InNi₃C_{0.5}/Ni-foam also shows favorable RWGS and CO₂-to-CH₃OH performances that are comparable with those seen with the InNi₃C_{0.5}/Al₂O₃/Al-fiber (Tables S8 and S9).

DISCUSSION

In summary, we have discovered an outstanding nano-intermetallic InNi₃C_{0.5} catalyst system via RWGS-reaction-oriented pre-design combined with atomistic-theoretical calculations and experimental verifications. Practical fiber/foam-structured InNi₃C_{0.5} nano-intermetallic catalysts engineered from nano- to macro-scale in one step have been developed, achieving unprecedented performance in the RWGS reaction and showing potential to catalyze CO₂ hydrogenation to CH₃OH. Most notably, such nano-intermetallic catalysts are also highly active, highly selective, and highly particularly stable for the DMO-to-EG process (EG synthesis using syngas derived from non-oil resources even from CO₂ through the RWGS reaction). We anticipate our essay to be a new point closer toward the ultimate goal of catalysis, namely, designing and tailoring the catalysts atom by atom with precise structure, and our findings might lead to commercial exploitation of such kind of nano-intermetallic catalysts for applications in highly efficient reduction of CO₂ to CO as well as carbonyl-to-hydroxyl transformation.

Limitations of the Study

The large-scale H₂ production should be from the renewable solar, hydraulic, and wind energy.

METHODS

All methods can be found in the accompanying [Transparent Methods supplemental file](#).

SUPPLEMENTAL INFORMATION

Supplemental Information can be found online at <https://doi.org/10.1016/j.isci.2019.07.006>.

ACKNOWLEDGMENTS

We acknowledge the financial supports from the National Natural Science Foundation of China (grants 21773069, 21703069, 21703137, 21473057, U1462129, 21273075), the Key Basic Research Project (grant 18JC1412100) and Shanghai Pujiang Program (grant 17PJ1403100) from the Shanghai Municipal Science and Technology Commission, and the National Key Basic Research Program (grant 2011CB201403) from the Ministry of Science and Technology of the People's Republic of China. We thank Prof. Dr. Roel Prins from the ETH Zurich for fruitful discussion.

AUTHOR CONTRIBUTIONS

P.C., G.Z., X.-R.S., and Y.L. conceived the idea for the project and designed the experiments; P.C., G.Z., X.-R.S., and Y.L. carried out the interpretation and wrote the manuscript; P.C., J.Z., and J.D. conducted the material synthesis, characterizations, and catalysis tests; P.C. and X.-R.S. performed the structural analysis and modeling; X.-R.S. carried out the DFT calculations; all authors discussed and commented on the manuscript; Y.L. directed the research.

DECLARATION OF INTERESTS

Y.L., P.C., J.Z., and G.Z. have a patent application related to this work filed with the Chinese Patent Office on 15 October 2017 (201710956080.1). The authors declare no competing interests.

Received: February 15, 2019

Revised: June 2, 2019

Accepted: July 1, 2019

Published: July 26, 2019

REFERENCES

- Aresta, M., Dibenedetto, A., and Angelini, A. (2014). Catalysis for the valorization of exhaust carbon: from CO₂ to chemicals, materials, and fuels. Technological use of CO₂. *Chem. Rev.* 114, 1709–1742.
- Armbrüster, M., Kovnir, K., Friedrich, M., Teschner, D., Wownick, G., Hahne, M., Gille, P., Szentmiklósi, L., Feuerbacher, M., Heggen, M., et al. (2012). Al₁₃Fe₄ as a low-cost alternative for palladium in heterogeneous hydrogenation. *Nat. Mater.* 11, 690–693.
- Chen, C.-S., Cheng, W.-H., and Lin, S.-S. (2001). Enhanced activity and stability of a Cu/SiO₂ catalyst for the reverse water gas shift reaction by an iron promoter. *Chem. Commun.* 1770–1771.
- Dou, J., Sheng, Y., Choong, C., Chen, L., and Zeng, H.C. (2017). Silica nanowires encapsulated Ru nanoparticles as stable nanocatalysts for selective hydrogenation of CO₂ to CO. *Appl. Catal. B* 219, 580–591.
- Federsel, C., Jackstell, R., and Beller, M. (2010). State-of-the-art catalysts for hydrogenation of carbon dioxide. *Angew. Chem. Int. Ed.* 49, 6254–6257.
- Fenton, D.M., and Steinwand, P.J. (1974). Noble metal catalysis. III. Preparation of dialkyl oxalates by oxidative carbonylation. *J. Org. Chem.* 39, 701–704.
- Gonçalves, R.V., Vono, L.L.R., Wojcieszak, R., Dias, C.S.B., Wender, H., Teixeira-Neto, E., and Rossi, L.M. (2017). Selective hydrogenation of CO₂ into CO on a highly dispersed nickel catalyst obtained by magnetron sputtering deposition: a step towards liquid fuels. *Appl. Catal. B* 209, 240–246.
- Graciani, J., Mudiyansele, K., Xu, F., Baber, A.E., Evans, J., Senanayake, S.D., Stacchiola, D., Liu, P., Hrbek, J., Sanz, J.F., and Rodriguez, J.A. (2014). Highly active copper-ceria and copper-ceria-titania catalysts for methanol synthesis from CO₂. *Science* 345, 546–550.
- Ji, X.L., Lee, K.T., Holden, R., Zhang, L., Zhang, J.J., Botton, G.A., Couillard, M., and Nazar, L.F. (2010). Nanocrystalline intermetallics on mesoporous carbon for direct formic acid fuel cell anodes. *Nat. Chem.* 2, 286–293.
- Karl, T.R., and Trenberth, K.E. (2003). Modern global climate change. *Science* 302, 1719–1723.
- Kondrat, S.A., Smith, P.J., Wells, P.P., Chater, P.A., Carter, J.H., Morgan, D.J., Fiordaliso, E.M., Wagner, J.B., Davies, T.E., Lu, L., et al. (2016). Stable amorphous georgeite as a precursor to a high-activity catalyst. *Nature* 531, 83–87.
- Kondratenko, E.V., Mul, G., Baltrusaitis, J., Larrazábal, G.O., and Pérez-Ramírez, J. (2013). Status and perspectives of CO₂ conversion into fuels and chemicals by catalytic, photocatalytic and electrocatalytic processes. *Energy Environ. Sci.* 6, 3112–3135.
- Larrazábal, G.O., Martín, A.J., Mitchell, S., Hauert, R., and Pérez-Ramírez, J. (2016). Synergistic effects in silver-indium electrocatalysts for carbon dioxide reduction. *J. Catal.* 343, 266–277.
- Li, Y.K., Zhang, Q.F., Chai, R.J., Cao, F.H., Liu, Y., and Lu, Y. (2015). Ni-Al₂O₃/Ni-foam catalyst with enhanced heat transfer for hydrogenation of CO₂ to methane. *AIChE J.* 61, 4323–4331.
- Mao, Y., Wang, H.F., and Hu, P.J. (2017). Theory and applications of surface micro-kinetics in the rational design of catalysts using density functional theory calculations. *WIREs Comput. Mol. Sci.* 7, e1321.
- Martin, O., Martin, A.J., Mondelli, C., Mitchell, S., Segawa, T.F., Hauert, R., Drouilly, C., Curulla-Ferré, D., and Pérez-Ramírez, J. (2016). Indium oxide as a superior catalyst for methanol synthesis by CO₂ hydrogenation. *Angew. Chem. Int. Ed.* 55, 6261–6265.
- Nicholson, K.M., Chandrasekhar, N., and Sholl, D.S. (2014). Powered by DFT: screening methods that accelerate materials development for hydrogen in metals applications. *Acc. Chem. Res.* 47, 3275–3283.
- Orr, J.C., Fabry, V.J., Aumont, O., Bopp, L., Doney, S.C., Feely, R.A., Gnanadesikan, A., Gruber, N., Ishida, A., Joos, F., et al. (2005). Anthropogenic ocean acidification over the twenty-first century and its impact on calcifying organisms. *Nature* 437, 681–686.
- Park, H., Choi, J., Kim, H., Hwang, E., Ha, D.H., Ahn, S.H., and Kim, S.K. (2017). AgIn dendrite catalysts for electrochemical reduction of CO₂ to CO. *Appl. Catal. B* 219, 123–131.
- Porosoff, M.D., and Chen, J.G. (2013). Trends in the catalytic reduction of CO₂ by hydrogen over supported monometallic and bimetallic catalysts. *J. Catal.* 301, 30–37.
- Porosoff, M.D., Yan, B.H., and Chen, J.G. (2016). Catalytic reduction of CO₂ by H₂ for synthesis of CO, methanol and hydrocarbons: challenges and opportunities. *Energy Environ. Sci.* 9, 62–73.
- Qin, Y.N., Luo, M.C., Sun, Y.J., Li, C.J., Huang, B.L., Yang, Y., Li, Y.J., Wang, L., and Guo, S.J. (2018). Intermetallic hcp-PtBi/fcc-Pt core/shell nanoplates enable efficient bifunctional oxygen reduction and methanol oxidation electrocatalysis. *ACS Catal.* 8, 5581–5590.
- Schumann, J., Eichelbaum, M., Lunkenbein, T., Thomas, N., Galván, C.Á., Schlögl, R., and Behrens, M. (2015). Promoting strong metal support interaction: doping ZnO for enhanced activity of Cu/ZnO:M (M = Al, Ga, Mg) catalysts. *ACS Catal.* 5, 3260–3270.
- Shima, A., Sakurai, M., Sone, Y., Ohnishi, M., and Abe, T. Development of a CO₂ reduction catalyst for the Sabatier reaction. In *Forty-Second International Conference on Environmental Systems* (San Diego, California, 2012): AIAA Paper No. 2012–3552. <https://doi.org/10.2514/6.2012-3552>.
- Stamenkovic, V.R., Fowler, B., Mun, B.S., Wang, G., Ross, P.N., Lucas, C.A., and Markovic, N.M. (2007). Improved oxygen reduction activity on Pt₃Ni(111) via increased surface site availability. *Science* 315, 493–497.
- Studt, F., Sharafutdinov, I., Abild-Pedersen, F., Elkjaer, C.F., Hummelshøj, J.S., Dahl, S., Chorkendorff, I., and Nørskov, J.K. (2014). Discovery of a Ni-Ga catalyst for carbon dioxide reduction to methanol. *Nat. Chem.* 6, 320–324.
- Su, X., Yang, X., Zhao, B., and Huang, Y. (2017). Designing of highly selective and high-temperature endurable RWGS heterogeneous catalysts: recent advances and the future directions. *J. Energy Chem.* 26, 854–867.
- Wang, B., Li, Y., Wu, N., and Lan, C.Q. (2008). CO₂ bio-mitigation using microalgae. *Appl. Microbiol. Biotechnol.* 79, 707–718.
- Wang, C.Z., Han, L.P., Chen, P.J., Zhao, G.F., Liu, Y., and Lu, Y. (2016). High-performance, low Pd-loading microfibrous-structured Al-fiber@ns-AlOOH@Pd catalyst for CO coupling to dimethyl oxalate. *J. Catal.* 337, 145–156.
- Wang, D., Xin, H.L., Hovden, R., Wang, H., Yu, Y., Muller, D.A., Disalvo, F.J., and Abruña, H.D. (2013). Structurally ordered intermetallic platinum-cobalt core-shell nanoparticles with enhanced activity and stability as oxygen reduction electrocatalysts. *Nat. Mater.* 12, 81–87.
- Wu, H.C., Chang, Y.C., Wu, J.H., Lin, J.H., Lin, I.K., and Chen, C.S. (2015). Methanation of CO₂ and reverse water gas shift reactions on Ni/SiO₂ catalysts: the influence of particle size on selectivity and reaction pathway. *Catal. Sci. Technol.* 5, 4154–4163.
- Xu, X., and Moulijn, J.A. (1996). Mitigation of CO₂ by chemical conversion: plausible chemical reactions and promising products. *Energy Fuels* 10, 305–325.
- Yang, X.L., Su, X., Chen, X.D., Duan, H.M., Liang, B.L., Liu, Q.G., Liu, X.Y., Ren, Y.J., Huang, Y.Q., and Zhang, T. (2017). Promotion effects of potassium on the activity and selectivity of Pt/zeolite catalysts for reverse water gas shift reaction. *Appl. Catal. B* 216, 95–105.
- Ye, J.Y., Liu, C.J., and Ge, Q.J. (2012). DFT study of CO₂ adsorption and hydrogenation on the In₂O₃ surface. *J. Phys. Chem. C* 116, 7817–7825.
- Yue, H.R., Zhao, Y.J., Ma, X.B., and Gong, J.L. (2012). Ethylene glycol: properties, synthesis, and applications. *Chem. Soc. Rev.* 41, 4218–4244.
- Zhang, X., Zhu, X.B., Lin, L.L., Yao, S.Y., Zhang, M.T., Liu, X., Wang, X.P., Li, Y.W., Shi, C., and Ma, D. (2017). Highly dispersed copper over β-Mo₂C as an efficient and stable catalyst for the reverse water gas shift (RWGS) reaction. *ACS Catal.* 7, 912–918.

ISCI, Volume 17

Supplemental Information

Nano-Intermetallic $\text{InNi}_3\text{C}_{0.5}$

Compound Discovered as a Superior

Catalyst for CO_2 Reutilization

Pengjing Chen, Guofeng Zhao, Xue-Rong Shi, Jian Zhu, Jia Ding, and Yong Lu

Supplemental Figures

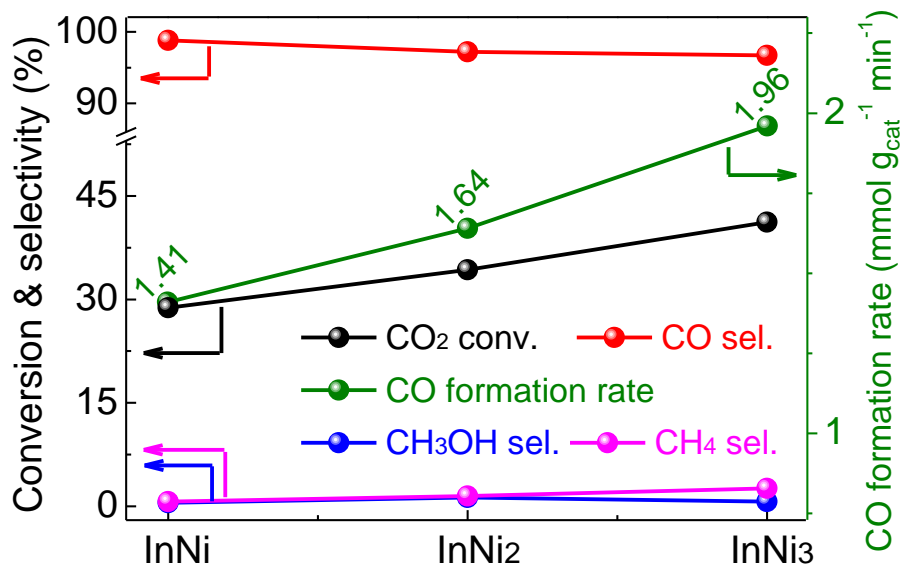


Figure S1. RWGS performance of intermetallic In-Ni catalysts, related to Figure 1. CO₂ conversion, product selectivity, and CO-formation rate for different catalysts (GHSV of 30,000 mL g_{cat}⁻¹ h⁻¹, 500 °C, H₂/CO₂/N₂ molar ratio of 66/22/12, 0.1 MPa).

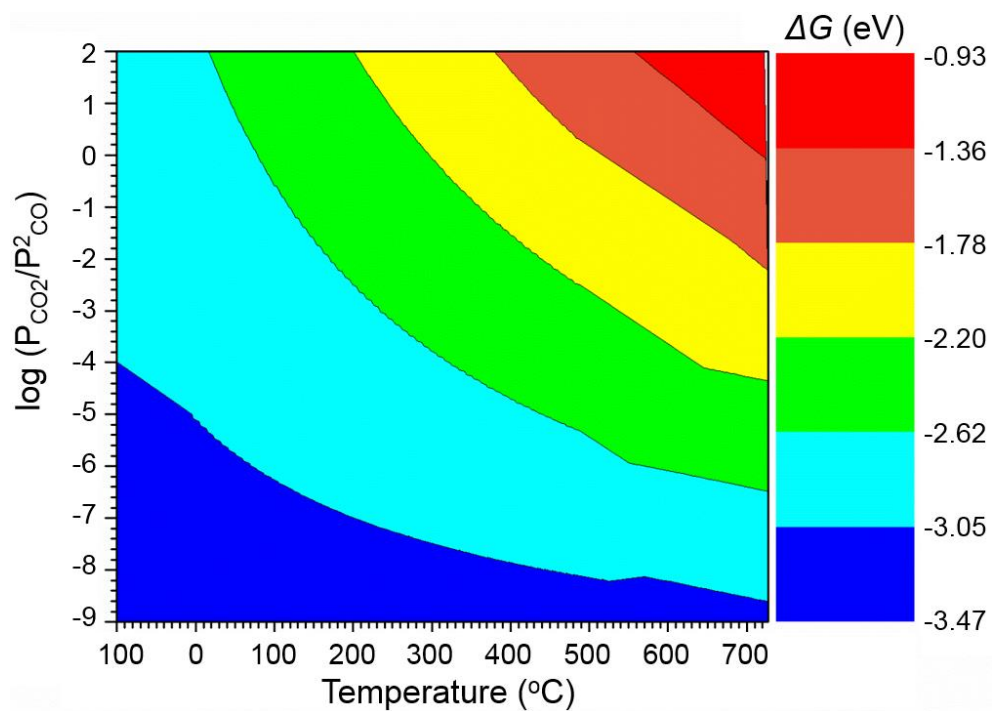


Figure S2. Gibbs free energies (ΔG) as a function of temperature and pressure for the carburization of InNi_3 in CO atmosphere ($2\text{InNi}_3 + 2\text{CO}_{(\text{g})} = 2\text{InNi}_3\text{C}_{0.5} + \text{CO}_{2(\text{g})}$), related to Figure 1.

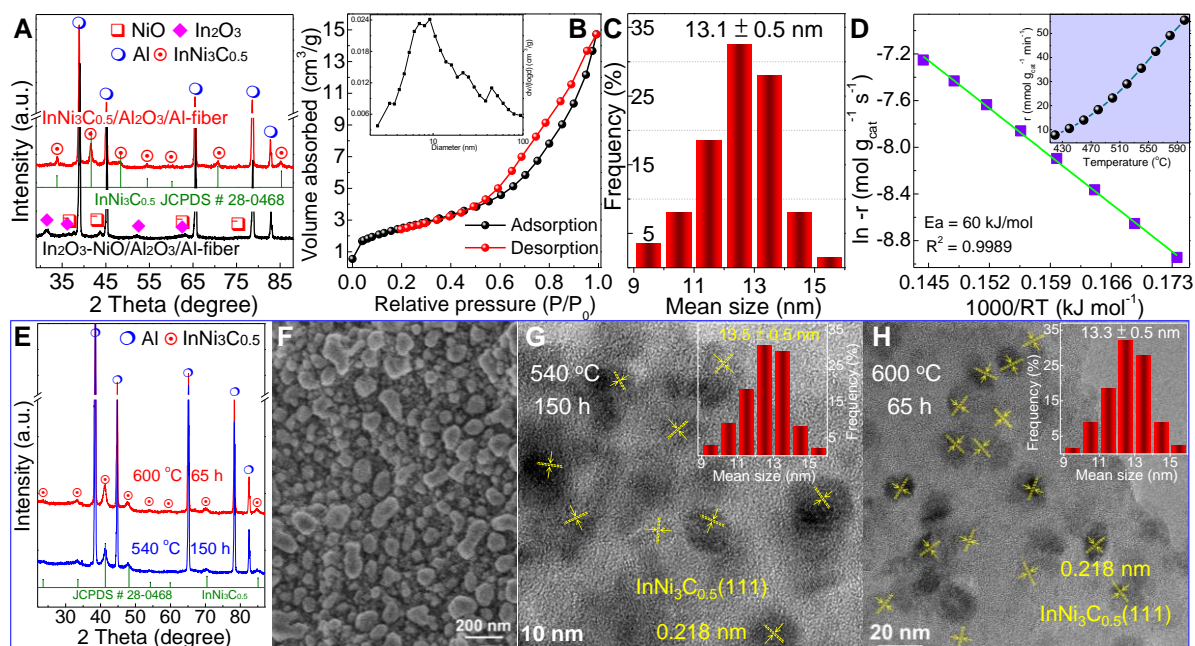


Figure S3. Geometry, apparent activation energy, morphology, and structural features of the thin-felt $\text{InNi}_3\text{C}_{0.5}/\text{Al}_2\text{O}_3/\text{Al}$ -fiber catalyst, related to Figure 2. (A) XRD patterns of the catalyst precursor of $\text{In}_2\text{O}_3\text{-NiO}/\text{Al}_2\text{O}_3/\text{Al}$ -fiber (black) and the fresh catalyst sample (red). (B) N_2 adsorption-desorption isotherms (insert: Barrett-Jovner-Halenda (BJH) mesopore size distribution) of the fresh catalyst sample. (C) Size distribution of the $\text{InNi}_3\text{C}_{0.5}$ nanoparticles of the fresh catalyst sample (corresponding to the TEM image in Figure 2C). (D) Arrhenius plot of the RWGS reaction for the $\text{InNi}_3\text{C}_{0.5}/\text{Al}_2\text{O}_3/\text{Al}$ -fiber catalyst (insert: CO-formation rate as a function of reaction temperature). $R^2 = 0.9989$ is the coefficient of determination of the linear regression fitting. Reaction conditions: $\text{H}_2/\text{CO}_2/\text{N}_2 = 66/22/12$, 1.0MPa, GHSV = 1,810,000 $\text{mL g}_{\text{cat}}^{-1} \text{h}^{-1}$. (E) XRD patterns of the used catalysts samples after stability testing under different conditions (blue: 540 °C, 54,000 $\text{mL g}_{\text{cat}}^{-1} \text{h}^{-1}$, and $\text{H}_2/\text{CO}_2/\text{N}_2 = 66/22/12$; red: 600 °C, 300,000 $\text{mL g}_{\text{cat}}^{-1} \text{h}^{-1}$, and $\text{H}_2/\text{CO}_2 = 66/37$). (F) SEM image of the used catalyst sample (150 h on stream). TEM images of the used catalysts samples after stability testing under different conditions: (G) 540 °C, 54,000 $\text{mL g}_{\text{cat}}^{-1} \text{h}^{-1}$, and $\text{H}_2/\text{CO}_2/\text{N}_2 = 66/22/12$; (H) 600 °C, 300,000 $\text{mL g}_{\text{cat}}^{-1} \text{h}^{-1}$, and $\text{H}_2/\text{CO}_2 = 66/37$, (inserts: size distribution of the $\text{InNi}_3\text{C}_{0.5}$ nanoparticles). **Note:** The N_2 adsorption-desorption isotherms and BJH size distribution in (B) reveal the mesoporous feature of the $\text{InNi}_3\text{C}_{0.5}/\text{Al}_2\text{O}_3/\text{Al}$ -fiber catalyst. The average TEM particle size in (C) was derived by statistical counting of 226 $\text{InNi}_3\text{C}_{0.5}$ -nanoparticles in the $\text{InNi}_3\text{C}_{0.5}/\text{Al}_2\text{O}_3/\text{Al}$ -fiber catalyst.

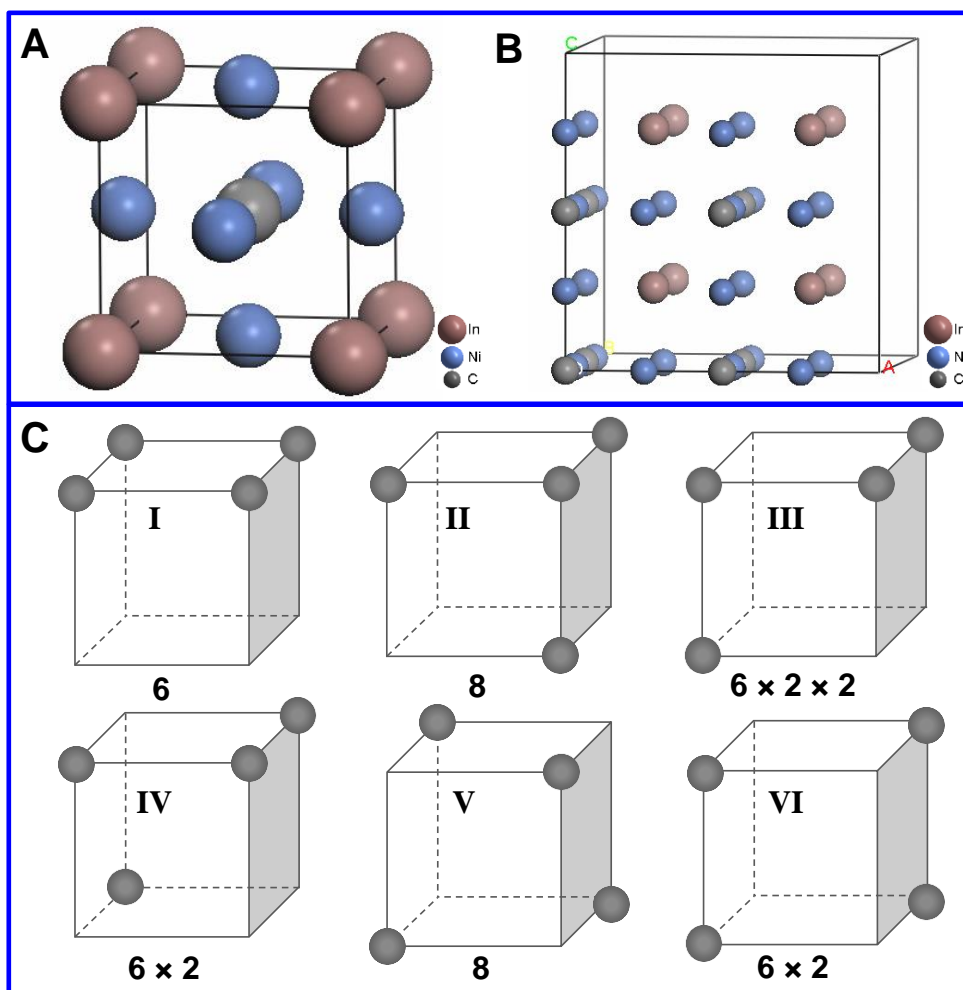


Figure S4. Distribution of four C atoms in the eight body-centers, related to Figure 3. (A) $1 \times 1 \times 1$ unit cell of InNi_3C . (B) $2 \times 2 \times 2$ super cell of $\text{In}_8\text{Ni}_{24}\text{C}_8$. (C) Six possible configurations for four C-atoms distribution. **Note:** A $1 \times 1 \times 1$ unit cell of InNi_3C was built, which contains one In atom and three Ni atoms, and the In and Ni positions can be identified with the corner-position of In atom and face-centered position of Ni atom (Figure S4A). Notably, this unit cell is composed of InNi_3C rather than $\text{InNi}_3\text{C}_{0.5}$. Subsequently, a $2 \times 2 \times 2$ super cell of $\text{In}_8\text{Ni}_{24}\text{C}_8$ was further built, which contains eight In atoms, twenty-four Ni atoms, and eight C atoms (Figure S4B). For the $\text{InNi}_3\text{C}_{0.5}$ intermetallic, however, this super cell contains eight In atoms, twenty-four Ni atoms, and four C atoms. Namely, there are only four C atoms occupy these eight body-centers. There are six possible configurations for the four C-atoms distribution. The most stable structure is shown as the “V” with the lowest energy (Figure S4C), which is also shown in Figure 3B. This kind of structure can be explained by the distribution of C atoms: the more even C atoms are distributed, the more stable the bulk structure is. In the “V” structure, four C atoms form a regular tetrahedron with each C-C distance of 5.345 Å.

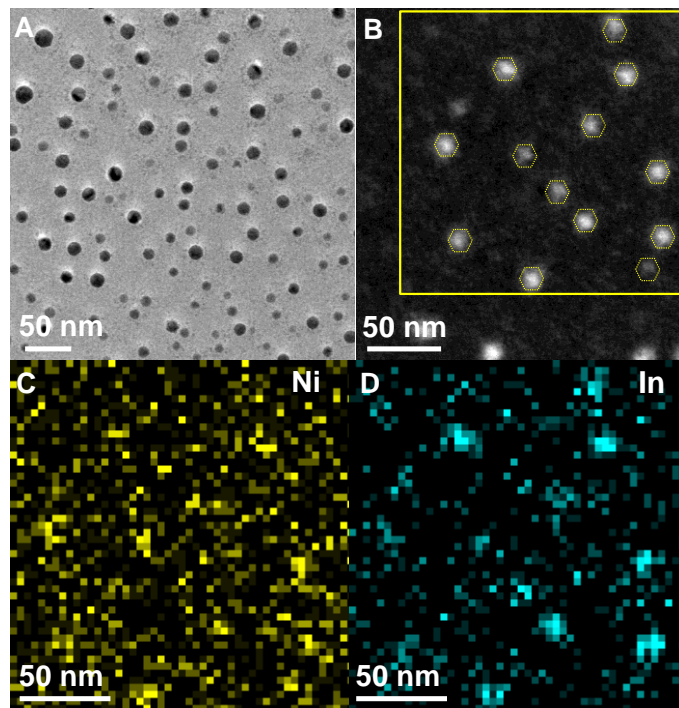


Figure S5. HAADF-STEM analysis, related to Figure 3. (A) Top view of TEM (A) and HAADF-STEM (B) images as well as the corresponding element mappings (C,D) of the $\text{InNi}_3\text{C}_{0.5}$ intermetallic catalyst.

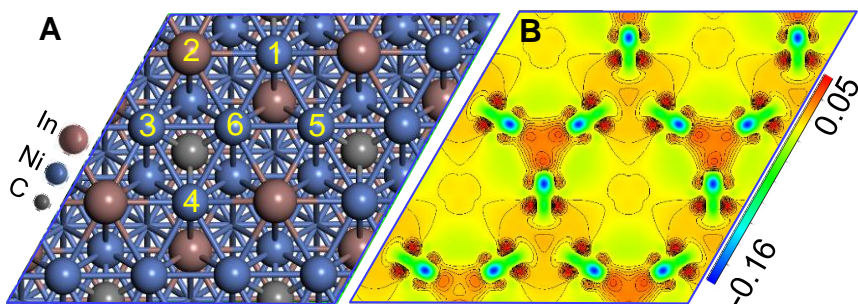


Figure S6. Calculation model and electronic property, related to Figure 4. (A) Top view of the In-Ni-terminated $\text{InNi}_3\text{C}_{0.5}(111)$ surface. (B) 2D view of the charge-density difference for C addition to form $\text{InNi}_3\text{C}_{0.5}(111)$, the cutting plane is the topmost Ni-atoms plane. Blue (negative value) and red (positive value) represent charge depletion and charge accumulation, respectively. The unit for the color scale bar is $e \text{ \AA}^{-3}$. The charge-density difference map shows that there is a degree of charge accumulation at the dual active sites (i.e., 3Ni-In and 3Ni-C) on the $\text{InNi}_3\text{C}_{0.5}(111)$ surface. The results reflect the fact that the dual active sites are potentially electron donors and much more nucleophilic than the other sites. As such, the dual active sites are more favorable for CO_2 activation than other sites on the $\text{InNi}_3\text{C}_{0.5}(111)$ surface.

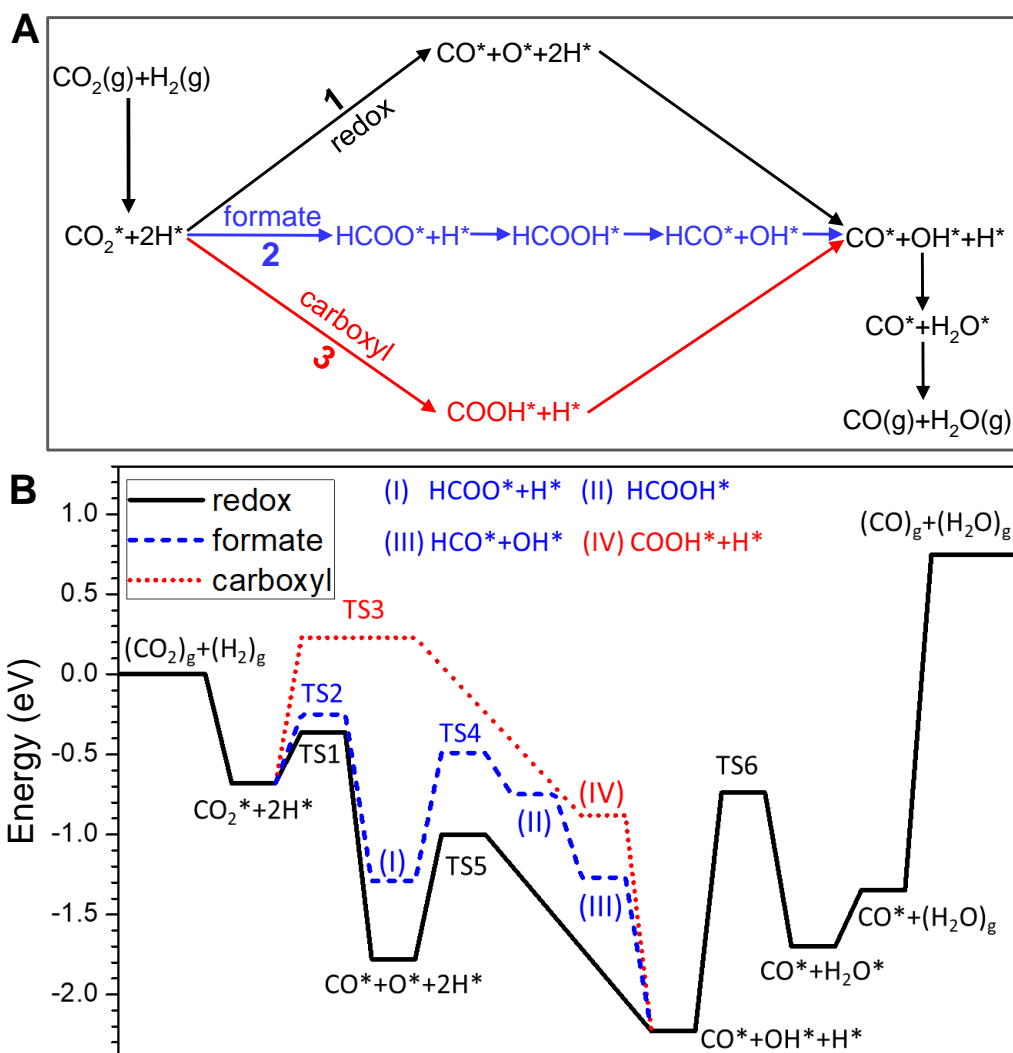


Figure S7. Possible typical pathways for the RWGS reaction on the $\text{InNi}_3\text{C}_{0.5}(111)$ surface, related to Figure 4. (A) Reaction mechanism network (Porosoff et al., 2016; Daza and Kuhn, 2016). Pathway 1, redox route; pathway 2, formate route; pathway 3, carboxyl route. (B) Energy profiles for possible pathways. The energies are reported relative to $\text{CO}_2(\text{g}) + \text{H}_2(\text{g})$. **Note:** CO_2^* dissociation or CO_2^* to HCOO^* and COOH^* ? The CO_2^* dissociated into O^* and CO^* is energetically favorable (with reaction energy E_r , -0.38 eV) and has a low activation barrier (E_a , 0.32 eV). The as-formed O^* is preferably adsorbed on h1 (3Ni-In) sites, and CO^* on h2 (3Ni-C) sites. In contrast, CO_2^* hydrogenation to formate (HCOO^*) or to carboxyl (COOH^*) will overcome much higher E_a (0.42 eV for HCOO^* and 0.75 eV for COOH^*). Clearly, the CO_2^* dissociation to CO^* and O^* (i.e., redox pathway) is preferred over the formate and carboxyl pathways on the $\text{InNi}_3\text{C}_{0.5}(111)$ surface. O^* react with H^* to form H_2O . The h1-adsorbed O^* reacts with H^* adsorbed at neighboring h2 site to form OH^* , which is also energetically favorable (-0.50 eV) and overcomes a relatively low E_a of 0.73 eV (Table S5). Once OH^* is formed, their combination occurs easily to form H_2O^* (this step is both thermodynamically and kinetically favorable as the reaction is exothermic with a small E_a of 0.25 eV), which is finally desorbed into gas phase (E_a , 0.35 eV).

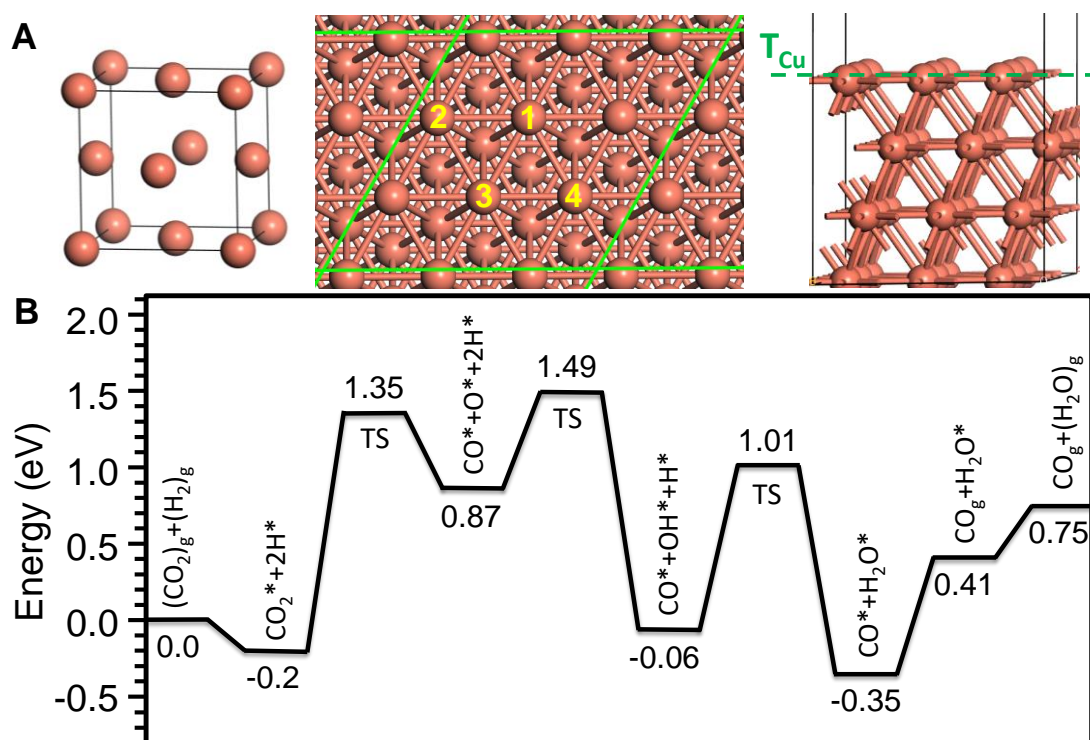


Figure S8. Crystal structure model of Cu and reaction pathways for the RWGS reaction, related to Figure 4. (A) Model of the optimized crystal structure of Cu(111) (left: crystal bulk structure model; middle: top view; right: side view). The reference data for Cu crystal structure is provided in [Table S10](#). The zone marked by the green dashed line on the stable surface (with the lowest surface free energy) is the surface slab structure unit. The atoms comprising the possible active sites in the zone are labeled by numbers. Green dashed line of T_{Cu} is the Cu termination. (B) Energy profiles for the most favorable pathways for the RWGS reaction on the Cu(111) surface. The energies are relative to $\text{CO}_2(\text{g}) + \text{H}_2(\text{g})$. Relevant adsorption configurations are provided in [Figure S9](#).

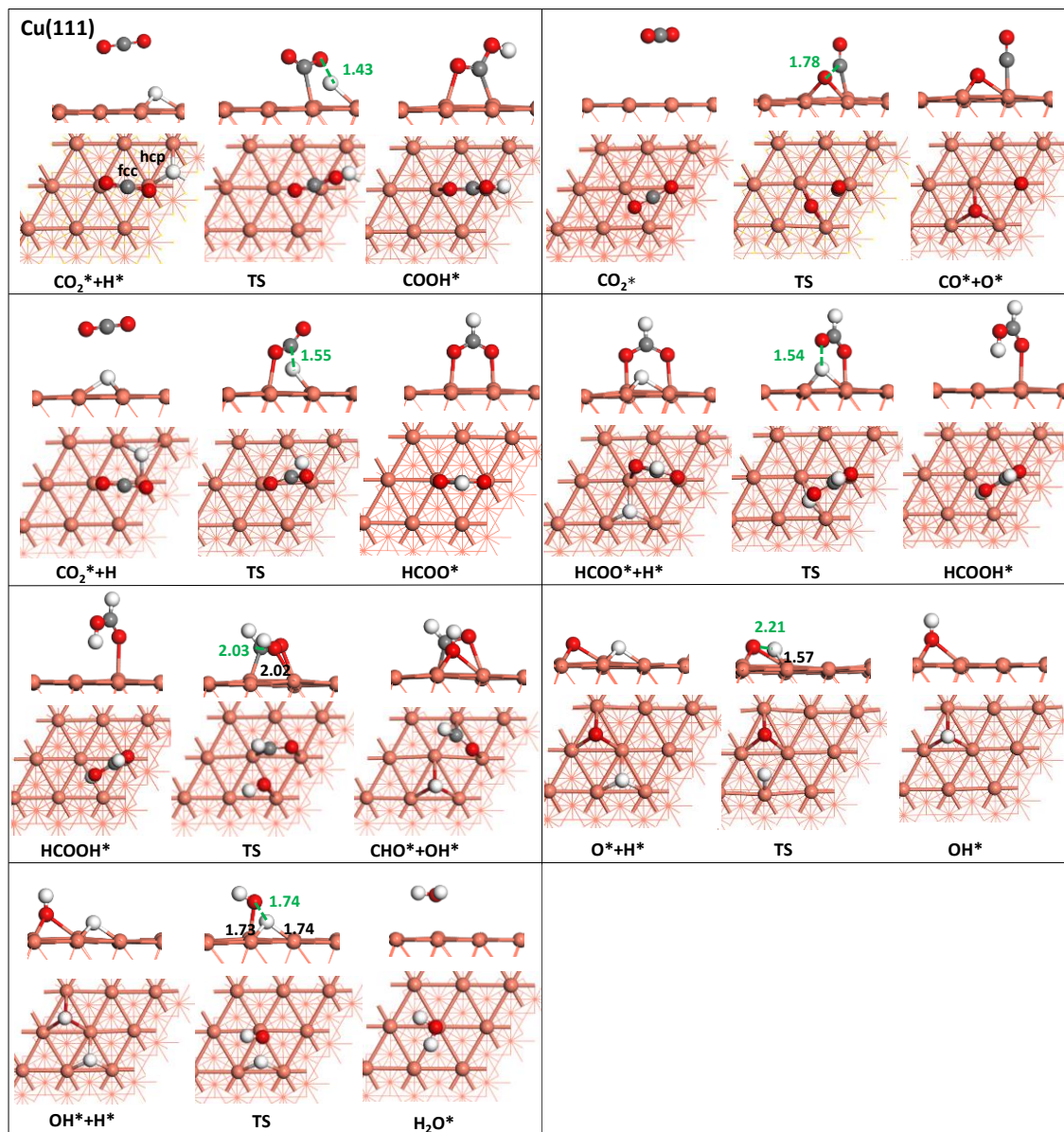


Figure S9. Elementary steps involved in the RWGS reaction on the Cu(111) surface, related to Figure 4 and Figure S8. The structures of initial, transition, and final states of all adsorbed species in each elementary step and the corresponding bond length (Å) are shown in this figure (top: side views, bottom: top views). C, H, O, and Cu atoms are shown in grey, white, red, and bronze spheres, respectively. The calculated reaction energies and activation barriers are given in [Table S11](#).

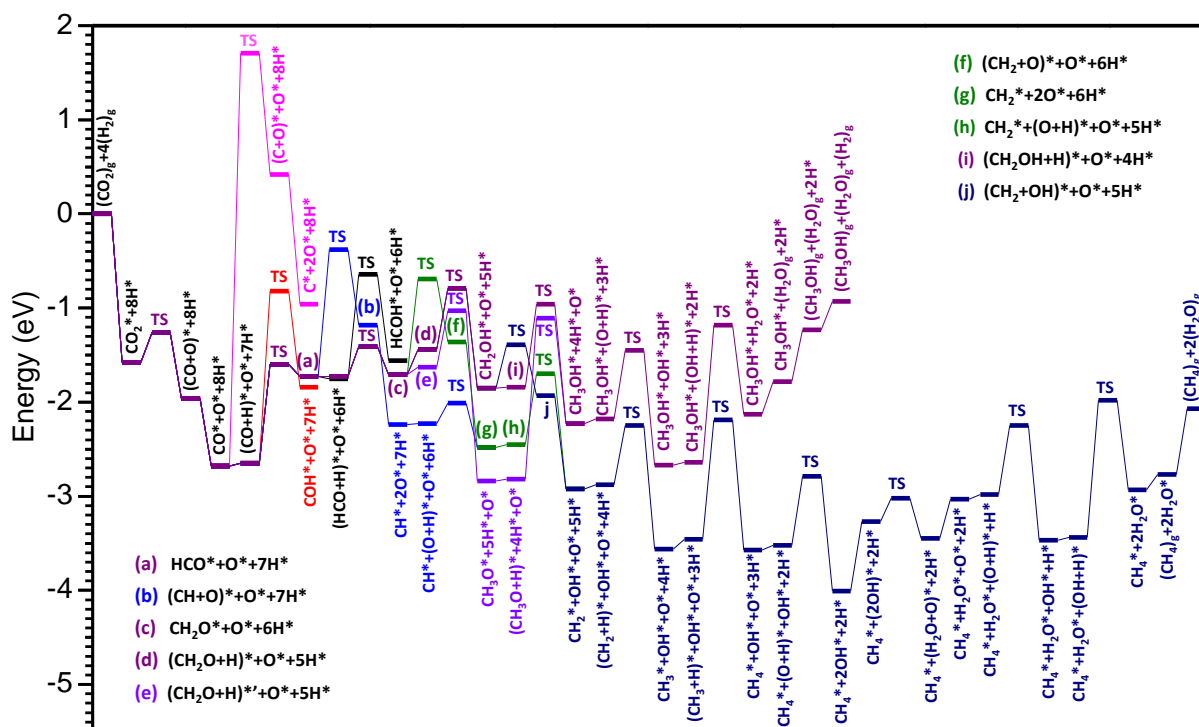


Figure S10. Energy profiles for CO₂ hydrogenation to CH₃OH and CH₄ on the InNi₃C_{0.5}(111) surface, related to Figure 4. For every elementary step, three possibilities were considered, including H addition to the C-end, H addition to the O-end, and C-O bond cleavage. The energies are reported relative to CO₂(g) + 4H₂(g). A* represents the adsorption state of A on the active sites at infinite separation and (A+B)* represents the most stable co-adsorption state of A and B. Relevant adsorption configurations are provided in Figure S11 and relevant reaction energies (E_r) and activation barriers (E_a) for each elementary step are provided in Table S5. The pathway in purple is the most favorable for the CO* hydrogenation to CH₂OH* and continuous hydrogenation to CH₃OH. The pathway in navy from the step of “CH₂OH*+O+5H*” is the most favorable for the CO₂* hydrogenation to CH₄. According to a much lower activation barrier in the competitive elementary steps, the most favorable pathways, for CH₃OH/CH₄ formation as well as CO-formation are shown in Figure 4C. To improve legibility, “H*” is omitted from the labels after the initial state. The pathway in purple is for the HCO* hydrogenation to CH₂OH* and continuous hydrogenation to CH₃OH*. The pathway in dark blue from the step of “CH₂OH* + O*” is for the CH₂OH* decomposition to CH₂* and continuous hydrogenation to CH₄*. The elementary steps in green are associated with the individual rate-limiting step in the corresponding pathway. **Note: Is CO* hydrogenated into CH₃OH or CH₄?** The generated CO* is either desorbed into the gas phase or further hydrogenated into CH₃OH and/or CH₄. **For CH₃OH formation**, the involved steps are as follows: CO* is first hydrogenated with H* to HCO* by overcoming an E_a of 1.05 eV, and this step is endothermic by +0.92 eV; subsequently, HCO* is hydrogenated to CH₂O* by overcoming a small E_a of 0.32 eV, and this step is endothermic by +0.02 eV; CH₂O* is hydrogenated into CH₂OH* (E_a , 0.65 eV), and this step is exothermic; CH₂OH* is further hydrogenated into CH₃OH* (E_a , 0.88 eV), and this step is also exothermic (E_r , -0.40 eV). Clearly, the rate-limiting step in CH₃OH formation on the InNi₃C_{0.5}(111) surface is CO*-to-HCO* with an E_a of 1.05 eV. **For CH₄ formation**, the involved steps are as follows: CO* is first hydrogenated with H* to HCO* by overcoming an E_a of 1.05 eV, and this step is endothermic by +0.92 eV; subsequently, HCO* is hydrogenated to CH₂O* by overcoming a small E_a of 0.32 eV, and this step is endothermic by +0.02 eV; for methanation, it is necessary to form CH_x* (x = 0-3) species form CH_xO* or CH_xOH* species via C-O bond scission, and the CH₂OH*

decomposition to CH_2^* has a significantly lower E_a of 0.46 eV (4.39 eV for CO^* -to- C^* , 1.35 eV for HCO^* -to- CH^* , 1.02 eV for CH_2O^* -to- CH_2^* , and 1.48 eV for CH_3O^* -to- CH_3^*) and is slightly exothermic with an E_r of -0.08 eV (+3.10 eV for CO^* -to- C^* , +0.55 eV for HCO^* -to- CH^* , +0.35 eV for CH_2O^* -to- CH_2^* , and +0.66 eV for CH_3O^* -to- CH_3^* , see detailed results in [Figure S10](#) and [Table S5](#)); CH_2^* further hydrogenation to CH_3^* is energetically favorable (E_r , -0.68 eV) and needs to overcome an E_a of 0.63 eV; the hydrogenation of CH_3^* to CH_4^* will overcome an E_a of 1.27 eV. Clearly, the rate-limiting step in the methanation on the $\text{InNi}_3\text{C}_{0.5}(111)$ surface is CH_3^* -to- CH_4^* with an E_a of 1.27 eV. The above comparison clearly suggests that CO^* is hydrogenated into CH_3OH (rate-limiting step E_a of 1.05 eV) rather than CH_4 (rate-limiting step E_a of 1.27 eV). Therefore, $\text{InNi}_3\text{C}_{0.5}$ has relatively higher methanol selectivity than methane selectivity. The results are consistent with the experimental results as well. Moreover, the generalized formation energy (E_f) can be employed to evaluate the adsorption strength of the reaction intermediates on $\text{InNi}_3\text{C}_{0.5}(111)$ surface (i.e., the smaller the value, the stronger the adsorption). E_f for CH_3O^* is 0.14 eV, 0.99 eV smaller than that for CH_2OH^* , indicating CH_3O^* is more stable than CH_2OH^* on the $\text{InNi}_3\text{C}_{0.5}(111)$ surface ([Table S4](#)). Therefore, the lower stability of CH_2OH^* makes itself a better intermediate for methanol synthesis than CH_3O^* , which has high stability and may not be efficient as transient species in the CH_2O^* -to- CH_3OH^* conversion. Consistently, this view is also reported in the available literature ([Graciani et al., 2014](#)), where authors showed that the high stability of formate (the intermediate over their catalyst) on the catalyst surface makes itself inefficient for CH_3OH synthesis. Therefore, it is rational to conclude that CO_2 hydrogenation to CH_3OH on the $\text{InNi}_3\text{C}_{0.5}(111)$ surface is through the CO^* -to- HCO^* -to- CH_2O^* -to- CH_2OH^* -to- CH_3OH^* pathway (see detailed results in [Table S5](#)).

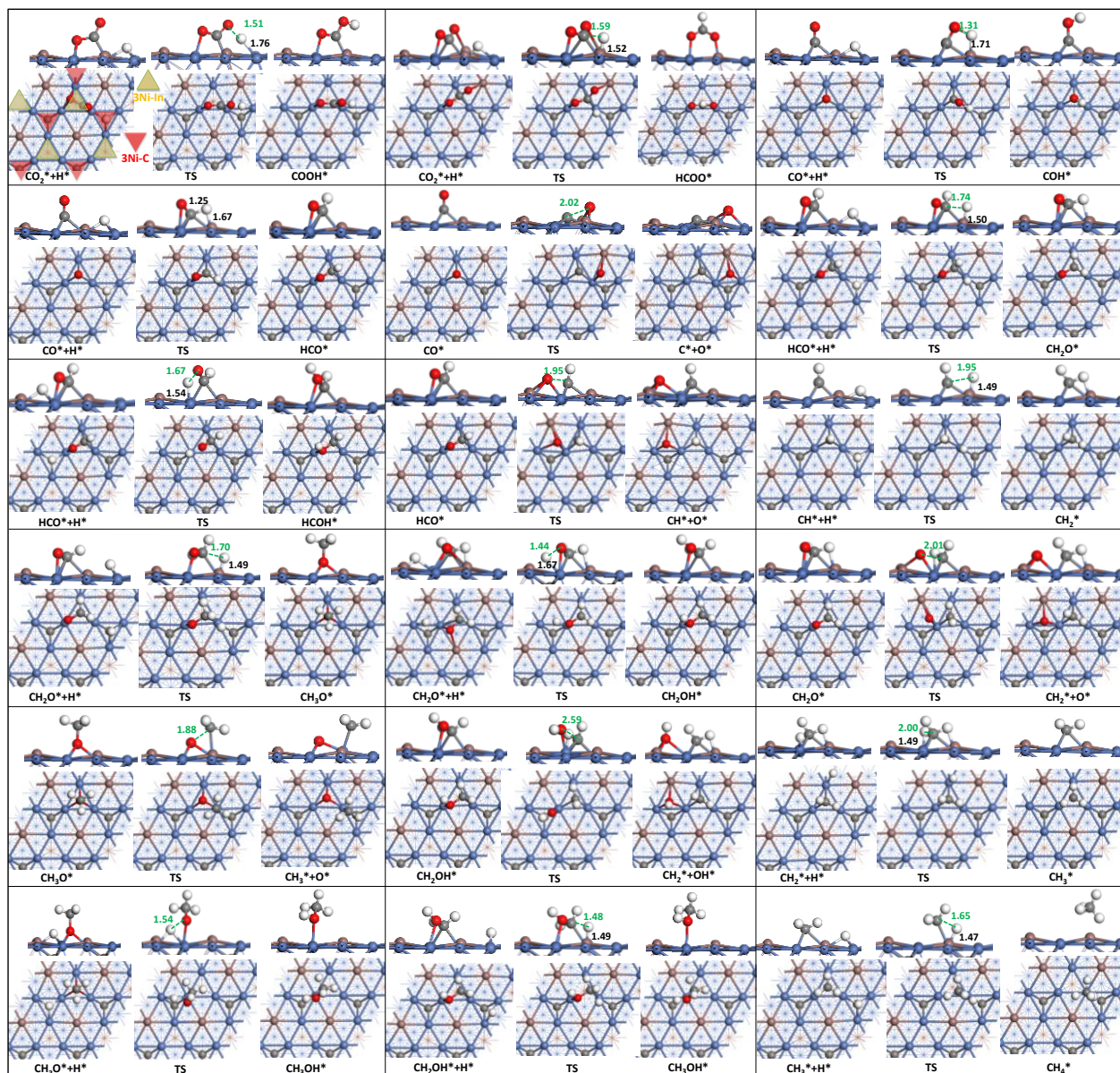


Figure S11. Elementary steps involved in CO₂ hydrogenation on the InNi₃C_{0.5}(111) surface, related to Figure 4. The configurations of initial, transition, and final states of all adsorbed species in each elementary step and the corresponding bond lengths (Å) are shown in this figure (top: side views, bottom: top views). C, H, O, In, and Ni atoms are shown in grey, white, red, bronze, and blue spheres, respectively. The calculated generalized formation energies (E_f) and geometric parameters of the intermediates are given in [Table S4](#). The calculated reaction energies and activation barriers for each step are given in [Table S5](#).

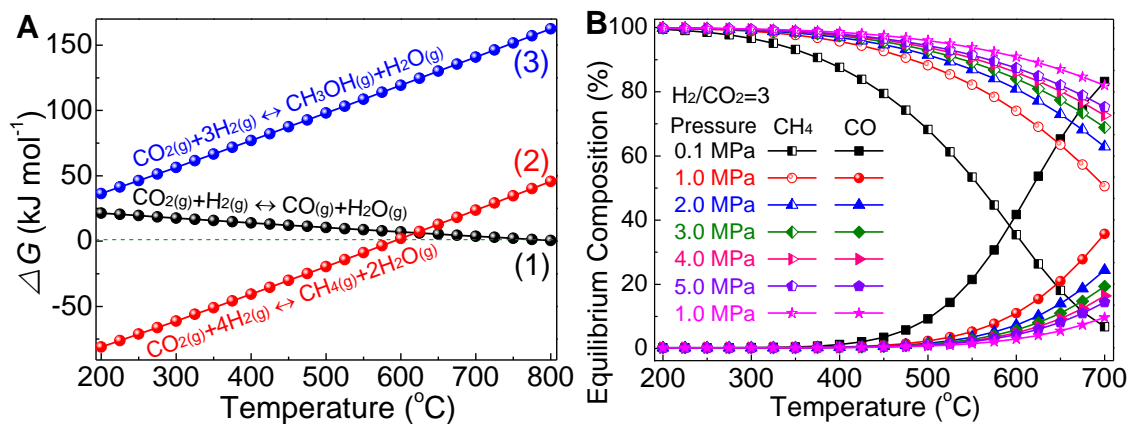


Figure S12. Thermodynamic analysis, related to Figure 4. (A) Gibbs free energies (ΔG) and (B) thermodynamic equilibrium composition of the main gaseous products of the RWGS reaction as a function of temperature with an initial stoichiometric H_2/CO_2 molar ratio of 3/1 and an amount of 100 moles of CO_2 at various reaction pressure (0.1-10 MPa).

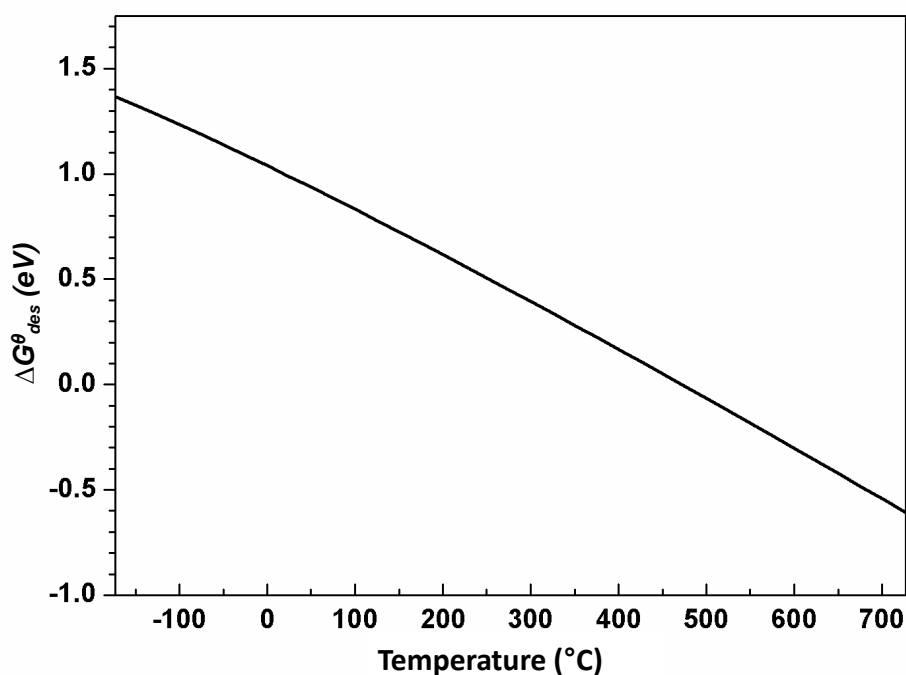


Figure S13. Standard Gibbs free energy ($\Delta G_{\text{des}}^{\theta}$) change of CO desorption from $\text{InNi}_3\text{C}_{0.5}(111)$ as the function of temperature, related to Figure 4. $\Delta G_{\text{des}}^{\theta}(\text{CO}) = \Delta E_{\text{des}}(\text{CO}) + G^{\theta}(\text{T})$, where $G^{\theta}(\text{T})$ includes the contributions from translation, vibration, and rotation of the CO molecule in gas phase. In this paper, $G^{\theta}(\text{T})$ is calculated by Dmol³ software (Delley, 1990; Delley, 2000). What to be noted is that increasing temperature is thermodynamically favorable for CO* desorption (Figure S12) due to the significant entropy contributions (Graciani et al., 2014) (that is, the smaller the $\Delta G_{\text{des}}^{\theta}(\text{CO})$, the easier the CO desorption). Therefore, CO* is preferentially desorbed into gas phase at our real RWGS temperature of 420-600 °C (Figure 2D-F).

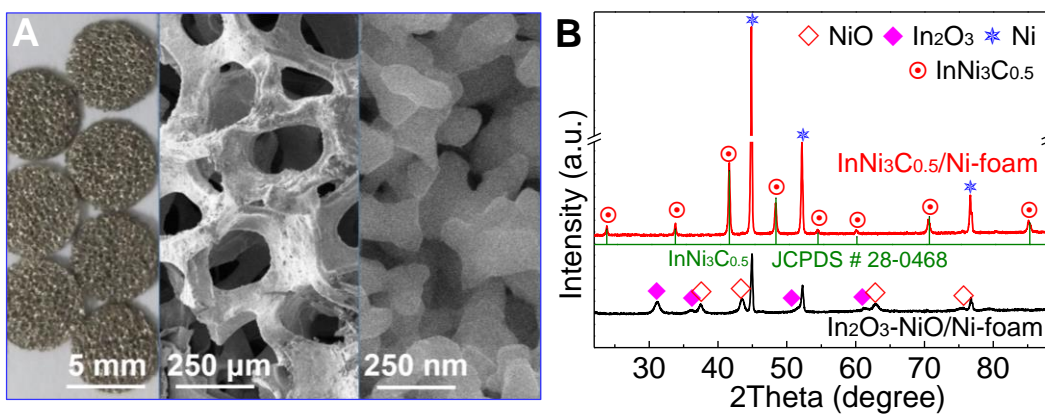


Figure S14. Structured InNi₃C_{0.5}/Ni-foam catalyst and its performance for the hydrogenation of DMO to EG, related to Table 1. (A) Optical photograph (left), low-magnitude SEM image (middle), and high-magnitude SEM image (right) of the InNi₃C_{0.5}/Ni-foam catalyst, showing the engineering of this catalyst at “macro-meso-nano” triple-scale levels. (B) XRD patterns of the In₂O₃-NiO/Ni-foam catalyst precursor (black) and InNi₃C_{0.5}/Ni-foam catalyst (red). The JCPDS profile (i.e., vertical lines) from the Joint Committee on Powder Diffraction File database is displayed for reference: InNi₃C_{0.5} (No. 28-0468).

Supplemental Tables

Table S1. Comparison of the InNi₃C_{0.5}/Al₂O₃/Al-fiber catalyst with the reported catalysts for RWGS reaction, related to Figure 2.

Catalyst	T (°C)	P (MPa)	H/C molar Ratio	GHSV (mL g _{cat} ⁻¹ h ⁻¹)	X _{CO₂} (%)	S _{CH₄} (%)	S _{CO} (%)	TOS ^a (h)	TOF (s ⁻¹)	Ref.
InNi ₃ C _{0.5} /Al ₂ O ₃ /Al-fiber	540	1.0	3.0	54,000	52.5	0.5	99.5	150	11.0	This work
1%Cu/ β -Mo ₂ C	600	0.1	2.0	300,000	38.5	0.8	99.2	40	N/A	Zhang et al., 2017
36%Cu/ZnO/Al ₂ O ₃	600	0.1	2.0	300,000	38.0	4	96	15	N/A	
10%Cu-0.3%Fe/SiO ₂	600	0.1	1.0	60,000	14.9	~1	~99	120	N/A	Wu et al., 2015
2.4%Ni/ <i>n</i> SiO ₂	660	0.1	4.0	40,000	67.5	1.3	98.7	40	N/A	Gonçalves et al., 2017
0.3%Pt/K ₈₀ -LTL zeolite	500	0.1	1.0	30,000	27.4	~0	~100	N/A	2.25 ^b	Yang et al., 2017
1.6%Ru@mSiO ₂ -N	400	0.1	4.0	15,000	23.0	61.5	83.5	50	0.053	Dou et al., 2017
0.4%Ru@mSiO ₂ -A	400	0.1	4.0	15,000	13.7	29.6	70.4	N/A	0.127	
Mo ₂ C	300	0.1	3.0	36,000	8.7	6.5	93.5	36	0.43	
7.5%Co-Mo ₂ C	300	0.1	3.0	36,000	9.5	2.0	98.0	36	0.27	Daza and Kuhn, 2016
Pt-Co/CeO ₂	300	0.1	3.0	36,000	6.6	18.2	81.8	N/A	0.24	
Cu-Ni/ γ -Al ₂ O ₃	600	0.1	1.0	2,000	28.7	20.3	79.7	N/A	N/A	Liu and Liu, 1999
Fe-Mo/ γ -Al ₂ O ₃	600	1.0	1.0	30,000	~35	~0	~100	60	N/A	Kharaji et al., 2013
6.2%Pd-3.6%Fe/SiO ₂	450	0.1	4.0	6,120	44.7	2.8	97.2	N/A	N/A	Park and McFarland, 2009
6.2%Pd-3.6%Ni/SiO ₂	450	0.1	4.0	6,120	50.5	89.0	11.0	N/A	N/A	

Table S1 (Continued)

Cu/Mo ₂ C	300	2.0	5.0	9,000	19	38.0	32.0	N/A	N/A	Xu et al., 2015
1%Ni/Mg(Al)O	700	0.1	3.0	540,000	~54	~6	~94	N/A	N/A	Rodrigues et al., 2017
0.1%Ir/TiO ₂	350	0.1	1.0	6,000	~2.1	~0	~100	N/A	N/A	Chen et al., 2017
Cu/Zn@C-submm	500	0.1	3.0	18,000	5.0	~0	~100	20	N/A	Zhang et al., 2017
Cu-Zn/AC	500	0.1	3.0	18,000	4.0	N/A	N/A	11	N/A	
4.5%Fe/ γ -Al ₂ O ₃	500	0.1	1.0	10,000	33.5	<1	>99	15	N/A	Loiland et al., 2016
4.2%Fe-3.4%K/ γ -Al ₂ O ₃	500	0.1	1.0	20,450	22.5	<1	>99	8	N/A	
Cu/ZnO (C-Z 40-60)	230	0.1	1.0	520	3.6	N/A	N/A	N/A	N/A	Galvan et al., 2016
2%K-Mo ₂ C/ γ -Al ₂ O ₃	300	2.1	3.0	7,560	11.7	~5	~95	68	N/A	Porosoff et al., 2017
Fe ₂ O ₃ nanowires	750	0.1	1.0	N/A	50	~0	~100	N/A	N/A	Fishman et al., 2017
Fe ₂ O ₃ nanosheets	510	0.1	1.0	N/A	30	~0	~100	N/A	N/A	
Ce _{1.1} Cu ₁	400	0.1	4.0	60,000	37	~0	100	10	N/A	Zhou et al., 2017
Cu-ZnGaZrO	325	0.1	3.0	3,000	16.8	0.3	99.7	N/A	N/A	Liu et al., 2017
NbC	300	0.1	2.0	36,000	2.09	0.5	94.5	N/A	1.0	Porosoff et al., 2015
Mo ₂ C	300	0.1	2.0	36,000	4.67	0.7	99.3	N/A	1.1	
WC	300	0.1	2.0	36,000	3.30	4.7	95.3	N/A	0.98	
1%Pt/TiO ₂	400	0.1	1.5	12,000	21	12	88	N/A	0.137	Kim et al., 2012
PtCo/TiO ₂	300	0.1	2.0	36,000	8.2	1.2	98.8	N/A	0.588	Kattel et al., 2016
PtCo/CeO ₂	300	0.1	2.0	36,000	9.1	7.7	92.3	N/A	0.333	Kattel et al., 2016
PtCo/ZrO ₂	300	0.1	2.0	36,000	7.8	10.5	89.5	N/A	0.267	Kattel et al., 2016

Table S1 (Continued)

CuFe/Al ₂ O ₃	700	0.1	1.0	60,000	42	N/A	N/A	10	N/A	Zhao et al., 2017
Pt-Co/MCF-17	300	0.55	3.0	60,000	~5	~0	~99	N/A	N/A	Alayoglu et al., 2011
(1%NiO/CeO ₂)/50% SBA-15	650	0.1	1.0	N/A	41.8	3.0	97.0	N/A	0.189	Alayoglu et al., 2015
	750	0.1	1.0	N/A	47.1	0	100	N/A	0.217	
	900	0.1	1.0	N/A	55.0	0	100	N/A	0.250	

^aTOS: time on stream.

^bThe experiment for TOF calculations was measured at 400 °C.

Table S2. Crystal structure and crystallographic information file of InNi₃C_{0.5}, related to Figure 3.

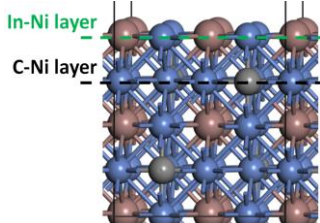
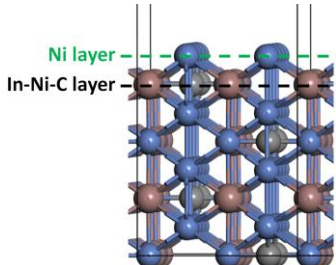
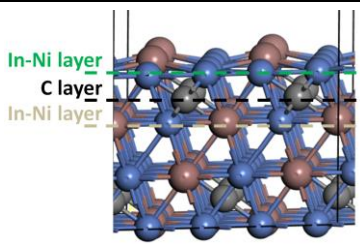
Crystal structure information	Space group number	Space group	International Crystal Structure Database (ICSD) reference (Tong et al., 2007; Saadaoui et al., 2015)					
			ICSD code	Crystal structure	a (Å)	b (Å)	c (Å)	
	221	$Fm\bar{3}m$	1897469	Cubic(<i>fcc</i>) ^a	3.780 (3.779) ^b	3.780 (3.779) ^b	3.780 (3.779) ^b	
Crystal element information	Name	Elem.	X	Y	Z	Biso.	S.O.F. ^c	Wyckoff
	C1	C	0.00000	0.00000	0.00000	0.5000	0.5000	1a
	In1	In	0.50000	0.50000	0.50000	0.5000	1.0000	1b
	Ni1	Ni	0.50000	0.00000	0.00000	0.5000	1.0000	3d

^aFace centred cubic (*fcc*) structure.

^bDFT calculated values.

^cSpatial occupied frequency.

Table S3. Surface free energies (γ , J m⁻²) of the selected surfaces with different terminations^a, related to Figure 4.

Surface	Structure (side view)	Termination ^b	Surface energy (J m ⁻²)
001 ^c		In-Ni	1.83
		C-Ni	1.91
011 ^d		Ni	2.16
		In-Ni-C	2.24
111 ^e		In-Ni ^f	1.66 ⁱ
		C ^g	2.19
		In-Ni ^h	2.25

^aSurface free energy is used to evaluate the stability of the surfaces with different terminations.

^bDifferent terminations of the corresponding surfaces.

^cInNi₃C_{0.5}(001) surface has two kinds of terminations: In-Ni layer and C-Ni layer.

^dInNi₃C_{0.5}(011) surface has two kinds of terminations: Ni layer and In-Ni-C layer.

^eThe periodic structure of InNi₃C_{0.5}(111) has three layers: In-Ni layer, C layer, and In-Ni layer (notably, this In-Ni layer followed by the next In-Ni layer rather than C layer).

^fInNi₃C_{0.5}(111) surface is terminated with In-Ni layer followed by C layer.

^gInNi₃C_{0.5}(111) surface is terminated with C layer followed by In-Ni layer.

^hInNi₃C_{0.5}(111) surface is terminated with In-Ni layer followed by the next In-Ni layer.

ⁱThe InNi₃C_{0.5}(111) surface with In-Ni termination and C sub-layer has the lowest γ of 1.66 J m⁻² among all the considered low-index surfaces with different terminations, which indicates that it has the highest stability, consistent with the fact that the InNi₃C_{0.5}(111) surface offers the strongest XRD-diffraction intensity and the most preferable exposure in TEM image (Figure 3A,D,E).

Table S4. Generalized formation energies (E_f) and optimized geometric parameters of the reaction intermediates on the $\text{InNi}_3\text{C}_{0.5}(111)$ surface, related to Figure 4.

Species	Site ^a	E_f (eV) ^b	Bond length (Å)
H*	h ₁ (h ₂)	-0.94(-0.12)	$d_{(\text{Ni-H})} = 1.73, 1.73, 1.73$ ($d_{(\text{Ni-H})} = 1.78, 1.78, 1.79$)
CO ₂ *	h ₁	1.70	$d_{(\text{Ni-C})} = 1.93/d_{(\text{Ni-O})} = 2.02, 2.03/d_{(\text{C-O})} = 1.37, 1.21$
CO*	h ₁ (h ₂)	0.75(1.42)	$d_{(\text{Ni-C})} = 1.98, 1.98, 1.98/d_{(\text{C-O})} = 1.20$ ($d_{(\text{Ni-C})} = 2.00, 2.00, 2.00/d_{(\text{C-O})} = 1.19$)
HCOO*	b1	0.95	$d_{(\text{Ni-O})} = 1.96, 1.96/d_{(\text{C-O})} = 1.27, 1.27$
HCOOH*	t ₁	1.34	$d_{(\text{Ni-C})} = 2.07/d_{(\text{C-O})} = 1.24, 1.21$
COOH*	h ₁	1.35 ^c 1.37 ^d	($d_{(\text{Ni-C})} = 2.03, 2.08/d_{(\text{Ni-O})} = 2.03/d_{(\text{C-O})} = 1.28, 1.37$) ^c ($d_{(\text{Ni-C})} = 1.89/d_{(\text{Ni-O})} = 2.01/d_{(\text{C-O})} = 1.27$) ^d
O*	h ₁	-0.14	$d_{(\text{Ni-O})} = 1.88, 1.88, 1.88$
OH*	h ₁	-0.73	$d_{(\text{Ni-O})} = 1.99, 1.99, 1.99$
H ₂ O*	t ₁	-0.34	$d_{(\text{Ni-O})} = 2.20$
HCO*	h ₁	1.55	$d_{(\text{Ni-C})} = 2.00, 2.02/d_{(\text{Ni-O})} = 1.97/d_{(\text{C-O})} = 1.30$
COH*	h ₁	1.44	$d_{(\text{Ni-C})} = 1.91, 1.92, 1.87/d_{(\text{C-O})} = 1.34$
CH ₂ O*	h ₁	1.42	$d_{(\text{Ni-C})} = 1.90/d_{(\text{Ni-O})} = 2.15, 2.15, 2.50/d_{(\text{C-O})} = 1.34$
HCOH*	h ₁	1.58 ^e 1.68 ^f	($d_{(\text{Ni-C})} = 1.97, 1.97, 2.09/d_{(\text{C-O})} = 1.39$) ^e ($d_{(\text{Ni-C})} = 1.97, 1.93/d_{(\text{Ni-O})} = 2.20/d_{(\text{C-O})} = 1.44$) ^f
CH ₃ O*	h ₁	0.14	$d_{(\text{Ni-O})} = 1.98, 1.99, 2.00/d_{(\text{C-O})} = 1.44$
CH ₂ OH*	h ₁	1.13	$d_{(\text{Ni-C})} = 2.05, 2.18/d_{(\text{Ni-O})} = 2.10/d_{(\text{C-O})} = 1.48$
CH ₃ OH*	t ₁	0.65	$d_{(\text{Ni-O})} = 2.14/d_{(\text{C-O})} = 1.45$
CH*	h ₁	1.19	$d_{(\text{Ni-C})} = 1.89, 1.90, 1.90$
CH ₂ *	h ₁	0.79	$d_{(\text{Ni-C})} = 1.97, 1.97, 2.04$
CH ₃ *	h ₁	0.00	$d_{(\text{Ni-C})} = 2.15, 2.15, 2.16$
CH ₄ *	Ph	-0.16	--

^aFigure 4A shows the detailed structures of these active sites: h1 is Hollow(3Ni-In), h2 is Hollow(3Ni-C), t1 is top(Ni), b1 is bridge(Ni-Ni). “ph” represents the physical adsorption.

^bGeneralized formation energies are relative to CH₄, H₂O, and H₂ in the gas phase (Medford et al., 2015). Such kind of energy can be employed to evaluate the adsorption strength of the reaction intermediates on $\text{InNi}_3\text{C}_{0.5}(111)$ surface. The smaller the value is, the stronger the adsorption. For the species i in the gas phase, $E_{f,i}$ is calculated according to the following equation: $E_{f,i} = (E_{total})_{f,i} - \sum_j n_j R_j$, where $E_{f,i}$ is the “generalized formation energy” of species i , $(E_{total})_{f,i}$ is the total energy of species i , n_j is the number of atomic species j in i , and R_j is the reference energy of

that atomic species. The reference energies (R_j) for each atomic species including atomic C, H and O are calculated by: $R_H = 0.5(E_{total})_{f,H_2}$, $R_C = (E_{total})_{f,CH_4} - 4R_H$, $R_O = (E_{total})_{f,H_2O} - 2R_H$. For the species i on the $\text{InNi}_3\text{C}_{0.5}(111)$ surface, $E_{f,i}$ is calculated by $E_{f,i} = (E_{total})_{f,i} - (E_{total})_{f, \text{clean-surface}} - \sum_j n_j R_j$, where $(E_{total})_{f, \text{clean-surface}}$ is the total energy of the clean $\text{InNi}_3\text{C}_{0.5}(111)$ surface.

^cCOOH* is in cis-form configuration on h1 site.

^dCOOH* is in trans-form configuration on h1 site.

^eHCOH* is adsorbed on h1 site with only C atom connecting with Ni.

^fHCOH* is adsorbed on h1 site with C and O atoms connecting with Ni.

Table S5. Reaction energies (E_r) and activation barriers (E_a) for each elementary step involved in the CO₂ hydrogenation on the InNi₃C_{0.5}(111) surface, related to Figure 4 and Figures S10,S11.

Entry	Elementary step	E_r (eV)		E_a (eV)	
		Dual sites ^a	Sole h1 sites ^b	Dual sites ^a	Sole h1 sites ^b
1 ^e	CO ₂ *+*→CO*+O*	-0.38	-1.10	0.32	0.32
2	CO*→CO _g +*	+1.36	+2.09	--	--
3 ^f	CO ₂ *+H*→HCOO*+*	-0.62(-0.61)	+0.19	0.42(0.43)	1.23
4 ^f	CO ₂ *+H*→COOH*+*	-0.36(-0.20)	+0.60	0.75(0.91)	1.71
5 ^f	O*+H*→OH*+*	-0.50(-0.44)	+0.35	0.73(0.79)	1.58
6 ^f	OH*+H*→H ₂ O*+*	+0.50(+0.53)	+1.33	1.45(1.49)	2.28
7	OH*+OH*→H ₂ O*+O*	-0.19 ^c	+0.56 ^d	0.25 ^c	0.99 ^d
8 ^f	CO*+H*→HCO*+*	+0.92(0.95)	+1.75	1.05(1.08)	1.88
9 ^f	CO*+H*→COH*+*	+0.81(+0.84)	+1.64	1.83(1.86)	2.66
10 ^f	HCO*+H*→HCOH*+*	+0.19(+0.17)	+0.98	1.11(1.09)	1.90
11 ^f	HCO*+H*→CH ₂ O*+*	+0.02(+0.02)	+0.81	0.32(0.32)	1.11
12 ^f	CH ₂ O*+H*→CH ₂ OH*+*	-0.41(-0.14)	+0.66	0.65(0.92)	1.73
13 ^f	CH ₂ O*+H*→CH ₃ O*+*	-1.21(-1.13)	-0.33	0.60(0.68)	1.48
14 ^f	CH ₃ O*+H*→CH ₃ OH*+*	+0.58(+0.60)	+1.41	1.71(1.73)	2.05
15 ^f	CH ₂ OH*+H*→CH ₃ OH*+*	-0.40(-0.38)	+0.43	0.88(0.90)	1.71
16 ^g	CO*+*→C*+O*	+3.10	+1.72	4.39	4.39
17 ^g	HCO*+*→CH*+O*	+0.55	-0.51	1.35	1.35
18 ^g	CH ₂ O*+*→CH ₂ *+O*	+0.35	-0.77	1.02	1.02
19 ^g	CH ₂ OH*+*→CH ₂ *+OH*	-0.08	-1.07	0.46	0.46

20 ^e	$\text{CH}_3\text{O}^{*+*} \rightarrow \text{CH}_3^{*+}\text{O}^*$	+0.66	-0.28	1.48	1.48
21 ^f	$\text{CH}^* + \text{H}^* \rightarrow \text{CH}_2^{*+*}$	-0.27(-0.26)	+0.54	0.22(0.23)	1.03
22 ^f	$\text{CH}_2^* + \text{H}^* \rightarrow \text{CH}_3^{*+*}$	-0.68(-0.64)	+0.16	0.63(0.67)	1.47
23 ^f	$\text{CH}_3^* + \text{H}^* \rightarrow \text{CH}_4^{*+*}$	-0.11(-0.01)	+0.79	1.27(1.37)	2.17

^a E_r and E_a correspond to the reactions that occur on dual active sites.

^b E_r and E_a correspond to the reactions that occur on sole h1 sites.

^c E_r and E_a correspond to the reaction that two OH* on dual active sites.

^d E_r and E_a correspond to the reaction that two OH* on sole h1 sites.

^eFor the steps in [entries 1,20](#), the O* preferably occupies the most favorite h1 sites while CO* and CH₃* preferably occupy h2 sites and Ni-top sites, respectively, ensuring that the species in this co-adsorption manner have the lowest energies.

^fFor the hydrogenation steps ([entries 3-6,8-15,21-23](#)), the intermediates are adsorbed on h1, and hydrogenated with the H* that is adsorbed on adjacent h2 sites (the E_r and E_a correspond to the data outside parentheses; there is an interaction between intermediates and H* for this case) or distant h2 sites (the E_r and E_a correspond to the data inside parentheses; there is no interaction between intermediates and H* for this case).

^gFor the steps in [entries 16-19](#), the CH_x* (x = 0-2) species preferably occupy the most favorite h1 sites while O* or OH* preferably occupy 2Ni-In sites, ensuring that the species in this co-adsorption manner have the lowest energies.

Table S6. CO₂ hydrogenation to methanol, catalyzed by the InNi₃C_{0.5}/Al₂O₃/Al-fiber catalyst^a, related to Figure 5.

T (°C)	CO ₂ Conv. (%)	Product Distribution (mol %)				STY _{MeOH} ^b (g _{MeOH} kg _{cat} ⁻¹ h ⁻¹)
		CH ₃ OH	CH ₄	CO	C ₂₊	
200	1.1	97.5	0	2.5	0.0	72.8
250	2.6	89.5	0	10.5	0.0	157.9
275	4.3	83.1	0.3	16.6	0.0	242.6
300	8.1	60.2	0.6	39.2	0.0	331.0

^aReaction conditions: 4.0 MPa, H₂/CO₂/N₂ molar ratio of 66/22/12, GHSV of 21,600 mL g_{cat}⁻¹ h⁻¹.

^bSTY_{MeOH} is the space time yield of CH₃OH.

Table S7. By-products selectivity for the hydrogenation of carbonyl compounds to alcohols catalyzed by the InNi₃C_{0.5}/Ni-foam catalyst, related to Table 1.

Substrate	Target product	By-product selectivity
DMO	EG	Methyl glycolate, 2-3%; Ethanol, <0.4%; Others (2-methoxyethanol, 2-ethoxyethanol, 1,2-propanediol, and 1,2-butanediol) 1-2%; Gaseous carbon-containing products (including methane, ethylene, ethane, and dimethyl ether), <0.1%
Acetone	Isopropanol	Propane, 1.0%
Furfural	Furfuryl alcohol	Tetrahydrofurfuryl alcohol, 3.9%; 2-methylfuran, 5.1%
Cyclohexanone	Cyclohexanol	Cyclohexane, 1.0%
Butanone	Butanol	Butane, 1.9%
Salicylaldehyde	Salicylol	Benzene and benzyl alcohol, 2.8%
<i>n</i> -Nonaldehyde	<i>n</i> -Nonyl alcohol	C ₃ -C ₇ alkanes, 4.9%

Table S8. Performance of the InNi₃C_{0.5}/Ni-foam catalyst for the RWGS reaction^a, related to Table 1.

T (°C)	CO ₂ Conv. (%)	Product Distribution (mol %)				r_{CO}^b (mmol g _{cat} ⁻¹ min ⁻¹)
		CH ₃ OH	CH ₄	CO	C ₂₊	
360	18.5	36.0	0.5	63.5	0.0	0.42
420	35.6	10.2	1.0	88.8	0.0	1.12
480	45.2	3.4	2.6	94.0	0.0	1.50
540	51.6	0.5	4.2	95.3	0.0	1.74

^aReaction conditions: 1.0 MPa, H₂/CO₂/N₂ molar ratio of 66/22/12, 21,600 mL g_{cat}⁻¹ h⁻¹.

^b r_{CO} is the formation rate of CO per gram catalyst per minute.

Table S9. CO₂ hydrogenation to methanol, catalyzed by the InNi₃C_{0.5}/Ni-foam catalyst^a, related to Table 1.

T (°C)	CO ₂ Conv. (%)	Product Distribution (mol %)				STY _{MeOH} ^b (g _{MeOH} kg _{cat} ⁻¹ h ⁻¹)
		CH ₃ OH	CH ₄	CO	C ₂₊	
200	0.9	98.5	0.0	1.5	0.0	60.2
250	2.5	94.2	0.6	5.2	0.0	159.9
275	4.9	83.6	1.0	15.4	0.0	278.1
300	7.8	57.6	1.8	40.6	0.0	305.0

^aReaction conditions: 4.0 MPa, H₂/CO₂/N₂ molar ratio of 66/22/12, 21,600 mL g_{cat}⁻¹ h⁻¹.

^bSTY_{MeOH} is the space time yield of CH₃OH.

Table S10. Reference data for Cu crystal structure in the present study, related to Figure 4 and Figure S8.

Chemical structure	Crystal structures		International Crystal Structure Database (ICSD) reference				
	Space group number	Space group	ICSD code	Crystal structure	a (Å)	b (Å)	c (Å)
Cu	225	$Fm\bar{3}m$	9008468	Cubic(<i>fcc</i>) ^a	3.615 (3.601) ^b	3.615 (3.601) ^b	3.615 (3.601) ^b

^aFace centred cubic (*fcc*) structure.

^bDFT calculated values.

1 **Table S11. Reaction energies (E_r) and activation barriers (E_a) for each elementary step**
 2 **involved in the RWGS reaction on the Cu(111) surface, related to Figure 4 and Figures**
 3 **S8,S9.**

4

Entry	Elementary step	E_r (eV)	E_a (eV)
1	$\text{CO}_2^{*+*} \rightarrow \text{CO}^{*} + \text{O}^{*}$	+1.06	1.55
2	$\text{CO}_2^{*} + \text{H}^{*} \rightarrow \text{COOH}^{*+*}$	+0.30	1.60
3	$\text{CO}_2^{*} + \text{H}^{*} \rightarrow \text{HCOO}^{*+*}$	-0.55	0.67
4	$\text{HCOO}^{*} + \text{H}^{*} \rightarrow \text{HCOOH}^{*+*}$	+0.11	0.79
5	$\text{HCOOH}^{*+*} \rightarrow \text{HCO}^{*} + \text{OH}^{*}$	+1.09	1.60
6	$\text{O}^{*} + \text{H}^{*} \rightarrow \text{OH}^{*+*}$	-0.92	0.62
7	$\text{OH}^{*} + \text{H}^{*} \rightarrow \text{H}_2\text{O}^{*+*}$	-0.27	1.07

5

6

1 **Transparent Methods**

2 **Preparation of catalysts**

3 **In-Ni nano-intermetallics.** The In-Ni nano-intermetallics (InNi, InNi₂, and InNi₃) were prepared
4 using nickel nitrate (Ni(NO₃)₂·6H₂O) and indium nitrate (In(NO₃)₃·2H₂O) as precursors by tuning
5 their corresponding molar ratios. Taking the InNi₃ synthesis as an example, In(NO₃)₃·2H₂O
6 (0.373 g) and Ni(NO₃)₂·6H₂O (0.873 g) were dissolved in distilled water (0.500 g), and the
7 solution was then continuously stirred at ambient temperature for 2 h followed by aging at
8 ambient temperature overnight and further at 100 °C for 24 h. The as-obtained sample was
9 calcined in static air at 400 °C for 2 h to obtain the In₂O₃-NiO precursor, which was directly
10 reduced in a quartz tube (inner diameter of 8 mm) in H₂ flow (flow rate of 30 mL min⁻¹) at
11 atmospheric pressure and 500 °C for 2 h. Finally, the InNi₃ nano-intermetallic was obtained. The
12 InNi and InNi₂ nano-intermetallics were synthesized by the same procedures via tuning the In:Ni
13 molar ratios.

14 **InNi₃C_{0.5} nano-intermetallic.** The as-prepared InNi, InNi₂, or InNi₃ was packed in a quartz tube
15 (inner diameter of 8 mm) and carburized in a simulated atmospheric reverse water-gas shift
16 (RWGS) stream of a mixture of H₂ and CO (60 mL min⁻¹, H₂:CO molar ratio of 2:1) at 500 °C for
17 2 h. The resulting product was slowly cooled to room temperature in a N₂ stream.

18 **InNi₃C_{0.5}/Al₂O₃/Al-fiber catalyst.** The microfibrillar-structured Al₂O₃/Al-fiber support was first
19 prepared from the thin-sheet (ca. 1.3 mm in thickness) 3D network structure of Al-fiber
20 (consisting of 10 vol% 60-μm Al-fiber and 90 vol% void volume) according to the method
21 described elsewhere (Wang et al., 2016). The as-prepared Al₂O₃/Al-fiber support was incipiently
22 impregnated with an aqueous solution of In(NO₃)₃·2H₂O and Ni(NO₃)₂·6H₂O (In:Ni molar ratio
23 of 1:3), followed by drying in air at 100 °C for 12 h and calcining in static air at 400 °C for 2 h to
24 obtain the catalyst precursor In₂O₃-NiO/Al₂O₃/Al-fiber. The In₂O₃-NiO/Al₂O₃/Al-fiber was
25 packed into a quartz tube (inner diameter of 8 mm) and reduced in a H₂ flow (30 mL min⁻¹) at 500
26 °C for 2 h and carburized at the same temperature in a simulated atmospheric RWGS stream of a
27 mixture of H₂ and CO (60 mL min⁻¹, H₂:CO molar ratio of 2:1) for 2 h.

28 **InNi₃C_{0.5}/Ni-foam catalyst.** The monolithic NiC₂O₄/Ni-foam was first prepared by the
29 hydrothermal method from the thin-sheet (ca. 1.1 mm in thickness) 3D network structure of Ni-
30 foam (110 pores per inch). Oxalic acid di-hydrate (H₂C₂O₄·2H₂O) and ammonium chloride
31 (NH₄Cl) were separately dissolved in deionized water, mixed together under continuous magnetic
32 stirring, and transferred into a stainless steel Teflon-lined autoclave of 100 mL capacity. The Ni-
33 foam was placed into the autoclave, which was then sealed and maintained at 150 °C for 2 h. The
34 as-obtained NiC₂O₄/Ni-foam was incipiently impregnated with an aqueous solution of
35 In(NO₃)₃·2H₂O followed by drying in air at 100 °C for 12 h and calcined in static air at 400 °C for
36 2 h to obtain the catalyst precursor In₂O₃-NiO/Ni-foam. The In₂O₃-NiO/Ni-foam was reduced and
37 carburized under the same conditions as the InNi₃C_{0.5}/Al₂O₃/Al-fiber catalyst.

38 **Characterization of catalysts**

39 **X-ray diffraction.** XRD measurements were conducted to analyze the structure and crystallinity
40 of the as-prepared nano-intermetallics and catalysts (i.e., InNi, InNi₂, InNi₃, InNi₃C_{0.5},
41 InNi₃C_{0.5}/Al₂O₃/Al-fiber, and InNi₃C_{0.5}/Ni-foam). The XRD patterns were collected on a Rigaku
42 Ultima IV diffractometer using a Cu Kα radiation source (λ = 1.5405 Å) operating at 35 kV and
43 25 mA in the 2θ angle range of 10-100 ° using a step size of 0.02 ° and at a scanning speed of 30 °
44 min⁻¹.

45 **Elemental analyses.** The In:Ni molar ratios of InNi, InNi₂, InNi₃, and InNi₃C_{0.5} were determined
46 to be 1:0.99, 1:2.01, 1:2.98, and 1:2.99, respectively, by inductively coupled plasma emission
47 spectrometry (ICP) on a Thermo IRIS Intrepid II XSP atomic emission spectrometer. Carbon
48 element analysis was performed on a PerkinElmer 2400 CHN elemental analyzer, and the In:Ni:C

1 molar ratio of $\text{InNi}_3\text{C}_{0.5}$ was determined to be 1:2.99:0.49. Moreover, the carbon content in
2 $\text{InNi}_3\text{C}_{0.5}$ was further confirmed by thermogravimetric analysis (TGA) on a Mettler-Toledo Model
3 TGA/SDTA851e apparatus. In the TGA measurement, the In_2O_3 -NiO mixture (10.0014 mg with
4 In:Ni molar ratio of 1:3) was reduced in H_2 flow at 500 °C for 2 h (these reduction conditions
5 ensure the full transformation of In_2O_3 -NiO into InNi_3 (8.0160 mg)), and the as-obtained InNi_3
6 was then carburized in a simulated atmospheric RWGS stream of H_2/CO mixture (60 mL min^{-1}
7 with $\text{H}_2:\text{CO}$ molar ratio of 2:1) at 500 °C for 2 h (these carburization conditions ensure the full
8 transformation of InNi_3 into $\text{InNi}_3\text{C}_{0.5}$ (8.1810 mg)). According to the weight increment from
9 InNi_3 to $\text{InNi}_3\text{C}_{0.5}$, the carbon content was determined to be 0.1650 mg, so that the In:Ni:C molar
10 ratio was determined to be 1:3:0.49, consistent with the above determined In:Ni:C molar ratio of
11 1:2.99:0.49.

12 **Transmission electron microscopy.** TEM measurements were performed on a Tecnai G² F30
13 high-resolution transmission electron microscope. The sample was suspended in ethanol by ultra-
14 sonication, and a drop of the suspension was deposited onto a holey carbon foil supported on a
15 copper grid. The grids were left to dry at room temperature prior to TEM measurements. The
16 accelerating voltage was 200 kV.

17 **Scanning electron microscopy.** SEM measurements were performed on a Hitachi S-4800
18 scanning electron microscope (Japan) with an accelerating voltage of 3.0 kV.

19 **Nitrogen adsorption-desorption.** Nitrogen adsorption-desorption isotherms were measured at -
20 196 °C on a Quantachrome Autosorb-3B instrument (USA). The samples were evacuated at 300
21 °C for at least 6 h before adsorption-desorption. The specific surface area (SSA) was calculated
22 from the adsorption branch in the range of relative pressure from 0.05 to 0.25 by the Brunauer-
23 Emmett-Teller (BET) method. The pore size distribution and total pore volume were determined
24 using the Barrett-Joyner-Halenda (BJH) model from the adsorption branch of the isotherms.

25 ***In-situ* Fourier transform infrared spectroscopy (FTIR).** *In-situ* FTIR experiments in the
26 continuous flow of $\text{H}_2/\text{CO}_2/\text{N}_2$ (molar ratio of 66/22/12) were recorded on a Nicolet NEXUS 6700
27 spectrometer (USA), equipped with a mercury-cadmium-telluride (MCT) detector and a high
28 temperature transmission cell rigged with CaF_2 windows. Spectra were acquired at a resolution of
29 4 cm^{-1} and 32 scans, and analyzed using OMNIC software. In a typical steady testing, the sample
30 was pressed to a wafer (13 mm in diameter) and placed into the cell chamber. The sample wafer
31 was pretreated at 400 °C for 2 h in the H_2 flow, flushed with highly purified N_2 at 400 °C for 1 h
32 and cooled down to 50 °C in N_2 for taking a reference spectrum. Then the reaction gas of
33 $\text{H}_2/\text{CO}_2/\text{N}_2$ (66/22/12) was introduced into the *in-situ* chamber at 50 °C and FTIR spectra were
34 recorded continuously for 32 scans with 2 spectra per minute until it reached steady state. For the
35 CO_2 hydrogenation, FTIR spectra were recorded continuously to capture dynamic change of the
36 surface species in the cell chamber temperature range from 50 to 325 °C with a ramping rate of
37 2 °C min^{-1} .

38 In order to analyze the composition of the products from *in-situ* FTIR experiment, all possible
39 carbonaceous species were detected by the on-line mass spectrometer (Proline Dycor, AMETEK
40 Process Instrument, USA) and the corresponding mass signals (intensities of ions with m/z of 44
41 (CO_2), 31 (CH_3OH), 28 (CO), and 16 (CH_4)) were recorded.

42 Evaluation of Catalysts

43 **Reverse water-gas shift reaction.** Catalysts were evaluated in a continuous flow fixed-bed
44 tubular reactor made of stainless steel with aluminum liner pipe (inner diameter of 8 mm with
45 length of 768 mm) that was heated by a furnace. Six thermocouples, located at the upper, middle,
46 and bottom of the furnace wall and reactor wall, were used to ensure the homogeneity of the
47 temperature in the reaction zone. In a typical catalyst evaluation, the circular chips of the
48 $\text{InNi}_3\text{C}_{0.5}/\text{Al}_2\text{O}_3/\text{Al}$ -fiber catalyst ($0.500 \pm 0.002 \text{ g}$) were packed layer-by-layer into the reactor.
49 The catalyst bed at the center of the reactor was supported by quartz wool at both ends, while the

1 remaining space was filled with quartz powder. Before evaluating their performance, the as-
 2 prepared catalysts were pre-treated in an atmospheric H₂ flow (30 mL min⁻¹) at 400 °C for 2 h.
 3 The reactant gas (H₂/CO₂/N₂ mixture with a molar ratio of 66/22/12 and N₂ as the internal
 4 standard) was introduced into the reactor using calibrated mass flow controllers. The reaction
 5 temperature, pressure, and gas hourly space velocity (GHSV) were varied in the range of 420-600
 6 °C, 1.0-4.0 MPa, and 21,600-54,000 mL g_{cat}⁻¹ h⁻¹, respectively. The catalyst stability was tested
 7 under severe RWGS reaction conditions: 540 °C, GHSV of 54,000 mL g_{cat}⁻¹ h⁻¹, H₂/CO₂/N₂ molar
 8 ratio of 66/22/12, and 1.0 MPa; 600 °C, GHSV of 300,000 mL g_{cat}⁻¹ h⁻¹, H₂/CO₂ molar ratio of
 9 66/33, and 0.1 MPa.

10 The product stream was quantitatively analyzed by an online Agilent 7820 gas chromatograph
 11 (GC) equipped with a flame ionization detector (FID) and thermal conductivity detector (TCD).
 12 The post-reactor line was heated to 120 °C to prevent product from condensing. All the data were
 13 collected after a given reaction time (at least 3 h) under steady-state conditions. A gas sample was
 14 withdrawn every 30 minutes, and more than eight-times measurements were taken for each
 15 reaction parameter. The products from this reaction were CO, CH₄, CH₃OH, C₂H₄, C₂H₆, and
 16 C₃H₈. The total content of C₂H₄, C₂H₆, and C₃H₈ was less than 0.1% and was, thus, neglected.
 17 The CO₂ conversion (%) and product selectivity (%) were calculated by the standard
 18 normalization method on the basis of carbon atom balance according to the following equations:

$$CO_2 \text{ conversion } (\%) = \left(1 - \frac{f_{CO_2} A_{CO_2, out}}{\sum f_i A_{i, out} + f_{CO_2} A_{CO_2, out}} \right) \times 100\%$$

$$i \text{ selectivity } (\%) = \left(\frac{f_i A_{i, out}}{\sum f_i A_{i, out}} \right) \times 100\%$$

19 where $A_{i, out}$ and f_i are the chromatographic peak area at the outlet and the relative molar
 20 calibration factor of the individual product i (i : CO, CH₄, and CH₃OH), respectively.

21 **Methanol synthesis.** The reaction apparatus, evaluation procedure, and product analyses for the
 22 methanol synthesis from CO₂ hydrogenation were the same as for the RWGS reaction described
 23 above. The reaction temperature was varied in the range of 200-300 °C at 4.0 MPa and GHSV of
 24 21,600 mL g_{cat}⁻¹ h⁻¹.

25 Space time yield of methanol (STY), expressed as grams of CH₃OH per kilogram catalyst per
 26 hour (g_{MeOH} kg_{cat}⁻¹ h⁻¹), was calculated according to the following equation:

$$CH_3OH \text{ STY} = \frac{F_{CO_2, in} \times X_{CO_2} \times S_{CH_3OH} \times MW_{CH_3OH}}{W_{cat} \times V_m}$$

27 where $F_{CO_2, in}$ is the volumetric flow rate (mL h⁻¹), X_{CO_2} is the CO₂ conversion, S_{CH_3OH} is the
 28 CH₃OH selectivity, MW_{CH_3OH} is the molecular weight of CH₃OH (32 g mol⁻¹), W_{cat} is the overall
 29 mass of catalyst (kg), and V_m is the ideal molar volume of CO₂ at standard temperature and
 30 pressure.

31 **Dimethyl oxalate (DMO) hydrogenation to ethylene glycol (EG).** Catalysts were evaluated in a
 32 continuous flow fixed-bed tubular stainless-steel reactor with 8 mm inner diameter. The
 33 InNi₃C_{0.5}/Ni-foam catalyst (0.500 ± 0.002 g) was loaded into the reactor and heated to the desired
 34 reaction temperature, and then H₂ was introduced into the reactor until the pressure was raised to
 35 the set points and the DMO methanol solution (13 wt%) was simultaneously introduced into the
 36 reactor. The DMO methanol solution was pumped using a high-pressure advection pump. The
 37 molar ratio of H₂ to DMO, weight hourly space velocity (WHSV_{DMO}), and reaction pressure were
 38 varied in the range of 45-180, 0.22-0.88 g_{DMO} g_{cat}⁻¹ h⁻¹, and 0.5-3.5 MPa, respectively. The
 39 catalyst stability was tested under the following conditions: 210 °C, molar ratio of H₂ to DMO of
 40 90, WHSV_{DMO} of 0.44 g_{DMO} g_{cat}⁻¹ h⁻¹, 2.5 MPa.

41 Only trace amounts (less than 0.1%) of gaseous carbon-containing products (methane,
 42 ethylene, ethane, and dimethyl ether) were formed, which were neglected in the product
 43 distribution calculations. The liquid effluent was collected and analyzed using a Shimadzu 2014C

1 GC with a FID detector and a HP-INNOWax column. The products from this reaction were EG,
2 methyl glycolate, ethanol, 2-methoxyethanol, 2-ethoxyethanol, 1,2-propanediol, and 1,2-
3 butanediol. The DMO conversion (%) and product selectivity (%) were calculated according to
4 the following equations:

$$DMO \text{ conversion } (\%) = \left(1 - \frac{f_{DMO}A_{DMO,out}}{\sum f_i A_{i,out} + f_{DMO}A_{DMO,out}} \right) \times 100\%$$

$$i \text{ selectivity } (\%) = \left(\frac{f_i A_{i,out}}{\sum f_i A_{i,out}} \right) \times 100\%$$

5 where $A_{i,out}$ and f_i are the chromatographic peak area at the outlet and the relative molar
6 calibration factor of the individual product i ($i =$ EG, methyl glycolate, ethanol, 2-methoxyethanol,
7 2-ethoxyethanol, 1,2-propanediol, and 1,2-butanediol), respectively.

8 Computational details

9 **Methods.** All spin-calculations were performed using the plane-wave-based periodic density
10 functional theory (DFT) method as implemented in the Vienna *ab initio* simulation package
11 (VASP), and the electron-ion interaction was described by the projector augmented wave (PAW)
12 method (Kresse and Furthmüller, 1996a; Kresse and Furthmüller, 1996b). To elucidate the role of
13 the van der Waals interaction in this system, we performed vdW-DF calculations using the
14 optB86b functional (Klimeš et al., 2010; Klimeš et al., 2011). The cutoff energy for the plane
15 wave basis set was fixed at 400 eV. Geometry optimization was performed with a conjugate-
16 gradient algorithm and considered to be converged when the forces on each unconstrained atom
17 was 0.03 eV/Å or less. The transition states were determined by the climbing-image nudged
18 elastic band method (CI-NEB) as implemented into VASP using the VTST tool set (Henkelman
19 et al., 2000; Sheppard et al., 2008). All the transition states were confirmed by vibrational
20 analysis to have only one imaginary frequency. Dipole correction was employed in all the
21 calculations.

22 The surface free energy (γ) was used to determine the thermodynamical stability of the
23 surfaces with different terminations and was calculated according to $\gamma = (E_{\text{slab}} - NE_{\text{bulk}})/A$, where
24 E_{slab} is the total energy of the slab, N is the number of the $\text{InNi}_3\text{C}_{0.5}$ units in the slab, E_{bulk} is the
25 bulk total energy per $\text{InNi}_3\text{C}_{0.5}$ unit, and A is the total surface area formed in cleavage (including
26 both slab sides).

27 Images of the Wulff equilibrium shape of the $\text{InNi}_3\text{C}_{0.5}$ crystal and electron density difference
28 were obtained using the VESTA software (Momma and Izumi, 2011).

29 **Models.** The $\text{InNi}_3\text{C}_{0.5}(111)$ surface was represented with a (2×2) cell of six layers where three
30 bottom layers were fixed to the bulk geometry while the upper layers together the adsorbates were
31 allowed to relax (Figure 4A). Cu(111) surface was modelled with a (3×3) surface unit cell of
32 four layer thicknesses (Figure S8A). During optimization, the top two layers together with the
33 adsorbed species were allowed to relax. The Monkhorst-Pack grids of $(3 \times 3 \times 3)$ and $(4 \times 4 \times 4)$
34 k -points were employed for the Cu and $\text{InNi}_3\text{C}_{0.5}$ bulk, respectively. The Monkhorst-Pack grids of
35 $(3 \times 3 \times 1)$ and $(4 \times 4 \times 1)$ k -points were employed for the Cu(111) and $\text{InNi}_3\text{C}_{0.5}(111)$ surfaces,
36 respectively. The vacuum spacing was greater than 15 Å to avoid cross-talk effects because of the
37 periodical repetition of the unit cells. The size of the unit cell, the thickness of the layers, and the
38 precision thresholds used in our calculations were carefully checked, and the structural parameters
39 and adsorption energies had high accuracies of 0.01 Å and 0.01 eV, respectively.

40 **Active sites analyses.** The zone marked by the green lines is the surface slab structure unit on the
41 corresponding stable surface (i.e., with the lowest surface free energy). The atoms comprising the
42 possible active sites in the corresponding zones are labeled by numbers (Figure 4A and Figure
43 S8A). As shown in Figure S8A, four kinds of active sites were established on the Cu(111) surface:
44 one top site (Cu1), one bridge site (Cu1-Cu2), one *fcc* site (Cu1-Cu3-Cu4), and one *hcp* site (Cu1-

Cu2-Cu3). Intermediates adsorbed on different sites: CO*, H₂O*, and HCOOH* were adsorbed at top sites; H*, O* and OH* were adsorbed at *fcc* sites; HCOO*, COOH*, and HCO* were adsorbed at bridge sites.

On the InNi₃C_{0.5}(111) surface (Figure 4A), nine kinds of active sites were established, including two top sites (Ni1, In2), three bridge sites (Ni1-Ni6, In2-Ni6, Ni3-Ni6), and four hollow sites (Ni1-Ni5-Ni6 (with one In atom right below), Ni1-In2-Ni6, In2-Ni3-Ni6 (with one Ni atom right below), Ni3-Ni4-Ni6 (with one C atom right below)). The sites in yellow/red-triangulations have stable adsorption for most intermediates on the InNi₃C_{0.5}(111) surface (Table S4).

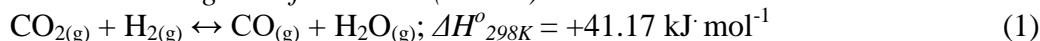
Reaction pathways. We used the most stably terminated InNi₃C_{0.5}(111) surface to investigate the surface reaction pathways for CO₂ hydrogenation. For the RWGS reaction, three possible reaction pathways including the redox, carboxyl (COOH) and formate (HCOO) routes were considered.

In order to explore the possibilities in CH₃OH/CH₄ formation from CO₂ hydrogenation on the InNi₃C_{0.5}(111) surface, DFT calculations were performed to examine the reaction pathways for the formation of CH₃OH and CH₄. For every elementary step, three possibilities were considered, including H addition to the C-end, H addition to the O-end, and C-O bond cleavage (Figure S10). The most favorable pathways, according to a much lower activation barrier in the competitive elementary steps, for CH₃OH/CH₄ formation as well as CO-formation were shown in Figure 4C.

Thermodynamic analysis. The thermodynamic analysis was conducted by using the HSC Chemistry 7.0 software, with the results shown in Figure S12. In the analysis, the temperature was increased from 200 to 700 °C. The species of H₂, CO₂, CO, H₂O, CH₄, and CH₃OH were simultaneously considered. The formation of CH₄ and CH₃OH was considered as unwanted side reactions.

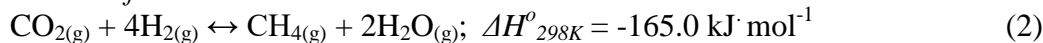
Main reaction

Reverse water-gas shift reaction (RWGS):



Side reaction

Methane formation reaction:



Methanol synthesis reaction:



Rate, turnover frequency of CO-formation, and apparent activation energy for RWGS reaction

CO-formation rate. CO-formation rate, expressed as micro-moles of produced CO per gram InNi₃C_{0.5}/Al₂O₃/Al-fiber catalyst per minute (mmol_{CO} g_{cat}⁻¹ min⁻¹), was calculated according to the equation:

$$r = \frac{F_{\text{CO}_2} \times X_{\text{CO}_2} \times S_{\text{CO}}}{V_m \times W_{\text{cat}}}$$

where F_{CO_2} is the flow rate of CO₂ (mL min⁻¹), X_{CO_2} is the CO₂ conversion, S_{CO} is the CO selectivity, V_m is the ideal molar volume of CO₂ at standard temperature and pressure, and W_{cat} is the mass of the InNi₃C_{0.5}/Al₂O₃/Al-fiber catalyst.

Turnover frequency of CO-formation. In order to assess the intrinsic activity of the InNi₃C_{0.5}/Al₂O₃/Al-fiber catalyst for the RWGS reaction, the specific turnover frequency (TOF) was measured (with CO₂ conversion of 7.3% at 540 °C, 1.0 MPa, and GHSV of 2,536,000 mL g_{cat}⁻¹ h⁻¹) and calculated, which was defined as the produced CO per active-site per second:

$$\text{TOF} = \frac{r}{\text{Active site number}} = \frac{\frac{F_{\text{CO}_2}}{V_m} \times X_{\text{CO}_2} \times S_{\text{CO}} \times N_A}{W_{\text{cat}} \times x \times N_{\text{num}}}$$

1 where F_{CO_2} is the flow rate of CO_2 ($mL s^{-1}$), X_{CO_2} is the CO_2 conversion, S_{CO} is the CO selectivity,
2 V_m is the ideal molar volume of CO_2 at standard temperature and pressure, N_A is the Avogadro
3 constant, W_{cat} is the mass of the $InNi_3C_{0.5}/Al_2O_3/Al$ -fiber catalyst, x is the $InNi_3C_{0.5}$ loading in the
4 $InNi_3C_{0.5}/Al_2O_3/Al$ -fiber catalyst, and N_{num} is the number of available surface active sites (i.e., the
5 total number of 3Ni-In and 3Ni-C) on per gram $InNi_3C_{0.5}$.

6 **Number of available surface active sites.** Assuming a uniform spherical shape of $InNi_3C_{0.5}$
7 nanoparticles, the specific surface area ($SA: m^2 g^{-1}$) of the $InNi_3C_{0.5}$ nanoparticles in the
8 $InNi_3C_{0.5}/Al_2O_3/Al$ -fiber catalyst was estimated based on their TEM-visualized particle size
9 according to the following equation (Gao et al., 2017):

$$SA = \frac{6}{\rho \times d_{InNi_3C_{0.5}}}$$

10 where ρ is the density of bulk $InNi_3C_{0.5}$. The corresponding TEM-visualized particle size
11 distribution of $InNi_3C_{0.5}$ nanoparticles is shown in **Figure S3C**.

12 Notably, the total area of the 3Ni-In and 3Ni-C sites accounted for 20.4% of the total surface
13 area of $InNi_3C_{0.5}(111)$ surface (**Figure 4A**). Assuming that all exposed surfaces of the supported
14 $InNi_3C_{0.5}$ nanoparticles were $InNi_3C_{0.5}(111)$ surface, the N_{num} was calculated according to the
15 following equation:

$$N_{num} = \frac{SA \times 20.4\%}{A_{(3Ni-In \text{ or } 3Ni-C)}}$$

16 where $A_{(3Ni-In \text{ or } 3Ni-C)}$ is the area of one 3Ni-In or 3Ni-C active-site (one 3Ni-In site has equal area
17 to one 3Ni-C site of $3.013 \times 10^{-20} m^2$).

18 **Apparent activation energy.** The activation energy (E_a) over the $InNi_3C_{0.5}/Al_2O_3/Al$ -fiber
19 catalyst was calculated based on the Arrhenius plot. According to the Arrhenius equation ($\ln-r =$
20 $\ln A - E_a/RT$), E_a is the slope estimated from the linear relationship of the Ln function of the CO
21 formation rate with the reciprocal of temperature. For the $InNi_3C_{0.5}/Al_2O_3/Al$ -fiber catalyst, the
22 RWGS reaction was performed under a kinetic-limiting region by controlling the temperature and
23 GHSV to maintain CO_2 conversion well below the equilibrium conversion (CO_2 conversion less
24 than 15%). Reaction conditions: $H_2/CO_2/N_2 = 66/22/12$, 1.0 MPa, GHSV of $1,940,000 mL g_{cat}^{-1} h^{-1}$,
25 and temperature in the 420-580 °C range.
26

Supplementary References

- Alayoglu, S., Beaumont, S. K., Zheng, F., Pushkarev, V. V., Zheng, H. M., Iablokov, V., Liu, Z., Guo, J. H., Kruse, N., and Somorjai, G. A. (2011). CO₂ hydrogenation studies on Co and CoPt bimetallic nanoparticles under reaction conditions using TEM, XPS and NEXAFS. *Top. Catal.* *54*, 778-785.
- Chen, X. D., Su, X., Su, H. Y., Liu, X. Y., Miao, S., Zhao, Y. H., Sun, K. J., Huang, Y. Q., and Zhang, T. (2017). Theoretical insights and the corresponding construction of supported metal catalysts for highly selective CO₂ to CO conversion. *ACS Catal.* *7*, 4613-4620.
- Daza, Y. A., and Kuhn, J. N. (2016). CO₂ conversion by reverse water gas shift catalysis: comparison of catalysts, mechanisms and their consequences for CO₂ conversion to liquid fuels. *RSC Adv.* *6*, 49675-49691.
- Delley, B. (1990). An all-electron numerical method for solving the local density functional for polyatomic molecules. *J. Chem. Phys.* *92*, 508-517.
- Delley, B. (2000). From molecules to solids with the Dmol³ approach. *J. Chem. Phys.* *113*, 7756-7764.
- Fishman, Z. S., He, Y. L., Yang, K. R., Lounsbury, A. W., Zhu, J. Q., Tran, T. M., Zimmerman, J. B., Batista, V. S., and Pfefferle, L. D. (2017). Hard templating ultrathin polycrystalline hematite nanosheets: effect of nano-dimension on CO₂ to CO conversion via the reverse water-gas shift reaction. *Nanoscale* *9*, 12984-12995.
- Galvan, C. A., Schumann, J., Behrens, M., Fierro, J. L. G., Schlogl, R., and Frei, E. (2016). Reverse water-gas shift reaction at the Cu/ZnO interface: Influence of the Cu/Zn ratio on structure-activity correlations. *Appl. Catal. B* *195*, 104-111.
- Gao, P., Li, S. G., Bu, X. N., Dang, S. S., Liu, Z. Y., Wang, H., Zhong, L. S., Qiu, M. H., Yang, C. G., Cai, J., Wei, W., and Sun, Y. H. (2017). Direct conversion of CO₂ into liquid fuels with high selectivity over a bifunctional catalyst. *Nat. Chem.* *9*, 1019-1024.
- Henkelman, G., Uberuaga, B. P., and Jónsson, H. (2000). A climbing image nudged elastic band method for finding saddle points and minimum energy paths. *J. Chem. Phys.* *113*, 9901-9904.
- Kattel, S., Yu, W., Yang, X. F., Yan, B. H., Huang, Y. Q., Wan, W. M., Liu, P., and Chen, J. G. (2016). CO₂ hydrogenation over oxide-supported PtCo catalysts: the role of the oxide support in determining the product selectivity. *Angew. Chem. Int. Ed.* *55*, 7968-7973.
- Kharaji, A. G., Shariati, A., and Takassi, M. A. (2013). A novel γ -alumina supported Fe-Mo bimetallic catalyst for reverse water gas shift reaction. *Chin. J. Chem. Eng.* *21*, 1007-1014.
- Kim, S. S., Lee, H. H., and Hong, S. C. (2012). A study on the effect of support's reducibility on the reverse water-gas shift reaction over Pt catalysts. *Appl. Catal. A Gen.* *423-424*, 100-107.
- Klimeš, J., Bowler, D. R., and Michaelides, A. (2010). Chemical accuracy for the van der Waals density functional. *J. Phys. Condens. Matter* *22*, 022201.
- Klimeš, J., Bowler, D. R., and Michaelides, A. (2011). Van der Waals density functionals applied to solids. *Phys. Rev. B* *83*, 195131.
- Kresse, G., and Furthmüller, J. (1996a). Efficiency of ab-initio total energy calculations for metals and semiconductors using a plane-wave basis set. *Comput. Mater. Sci.* *6*, 15-50.
- Kresse, G., and Furthmüller, J. (1996b). Efficient iterative schemes for ab initio total-energy calculations using a plane-wave basis set. *Phys. Rev. B* *54*, 11169-11186.

- 1 Liu, X. Y., Piscina, P. R. D. L., Toyir, J., and Homs, N. (2017). CO₂ reduction over Cu-ZnGaMO
2 (M = Al, Zr) catalysts prepared by a sol-gel method: Unique performance for the RWGS reaction.
3 *Catal. Today* 296, 181-186.
- 4 Liu, Y., and Liu, D. Z. (1999). Study of bimetallic Cu-Ni/ γ -Al₂O₃ catalysts for carbon dioxide
5 hydrogenation. *Int. J. Hydrogen Energy* 24, 351-354.
- 6 Loiland, J. A., Wulfers, M. J., Marinkovic, N. S., and Lobo, R. F. (2016). Fe/ γ -Al₂O₃ and Fe-K/ γ -
7 Al₂O₃ as reverse water-gas shift catalysts. *Catal. Sci. Technol.* 6, 5267-5279.
- 8 Lu, B. W., Ju, Y. W., Abe, T., and Kawamoto, K. (2015). Dispersion and distribution of
9 bimetallic oxides in SBA-15, and their enhanced activity for reverse water gas shift reaction.
10 *Inorg. Chem. Front.* 2, 741-748.
- 11 Medford, A. J., Shi, C., Hoffmann, M. J., Lausche, A. C., Fitzgibbon, S. R., Bligaard, T. and
12 Nørskov, J. K. (2015). CatMAP: A software package for descriptor-based microkinetic mapping
13 of catalytic trends. *Catal. Lett.* 145, 794-807.
- 14 Momma, K., and Izumi, F. (2011). VESTA 3 for three-dimensional visualization of crystal,
15 volumetric and morphology data. *J. Appl. Cryst.* 44, 1272-1276.
- 16 Park, J. N., and McFarland, E. W. (2009). A highly dispersed Pd-Mg/SiO₂ catalyst active for
17 methanation of CO₂. *J. Catal.* 266, 92-97.
- 18 Porosoff, M. D., Baldwin, J. W., Peng, X., Mpourmpakis, G., and Willauer, H. D. (2017).
19 Potassium-promoted molybdenum carbide as a highly active and selective catalyst for CO₂
20 conversion to CO. *ChemSusChem* 10, 2408-2415.
- 21 Porosoff, M. D., Kattel, S., Li, W. H., Liu, P., and Chen, J. G. (2015). Identifying trends and
22 descriptors for selective CO₂ conversion to CO over transition metal carbides. *Chem. Comm.* 51,
23 6988-6991.
- 24 Rodrigues, M. T., Zonetti, P. C., Alves, O. C., Souza-Aguiar, E. F., Borges, L. E. P., and Appel, L.
25 G. (2017). RWGS reaction employing Ni/Mg (Al, Ni) O - The role of the O vacancies. *Appl.*
26 *Catal. A Gen.* 543, 98-103.
- 27 Saadaoui, F., Khodja, F. Z. D., Kadoun, A. E. D., Khodja, M. D., Elias, A., and Boudali, A.
28 (2015). First-principles calculations of structural, elastic, thermodynamic, and electronic
29 properties of anti-perovskites A^{III}CNi₃ (A^{III} = Al, Ga, In). *Eur. Phys. J. B* 88, 316.
- 30 Sheppard, D., Terrell, R., and Henkelman, G. (2008). Optimization methods for finding minimum
31 energy paths. *J. Chem. Phys.* 128, 134106-10.
- 32 Tong, P., Sun, Y. P., Zhu, X. B., and Song, W. H. (2007). Synthesis and physical properties of
33 antiperovskite-type compound In_{0.95}CNi₃. *Solid State Commun.* 141, 336-340.
- 34 Xu, W. Q., Ramirez, P. J., Stacchiola, D., Brito, J. L., and Rodriguez, J. A. (2015). The
35 carburization of transition metal molybdates (M_xMoO₄, M = Cu, Ni or Co) and the generation of
36 highly active metal/carbide catalysts for CO₂ hydrogenation. *Catal. Lett.* 145, 1365-1373.
- 37 Zhang, J. Z., An, B., Hong, Y. H., Meng, Y. P., Hu, X. F., Wang, C., Lin, J. D., Lin, W. B., and
38 Wang, Y. (2017). Pyrolysis of metal-organic frameworks to hierarchical porous Cu/Zn-
39 nanoparticle @ carbon materials for efficient CO₂ hydrogenation. *Mater. Chem. Front.* 1, 2405-
40 2409.
- 41 Zhao, K., Bkour, Q., Hou, X. X., Kang, S. W., Park, J. C., Norton, M. G., Yang, J., and Ha, S.
42 (2017). Reverse water gas shift reaction over CuFe/Al₂O₃ catalyst in solid oxide electrolysis cell.
43 *Chem. Eng. J.* 336, 20-27.

1 Zhou, G. L., Dai, B. C., Xie, H. M., Zhang, G. Z., Xiong, K., and Zheng, X. X. (2017). CeCu
2 composite catalyst for CO synthesis by reverse water-gas shift reaction: Effect of Ce/Cu mole
3 ratio. *J. CO₂ Util.* *21*, 292-301.